NASA TECHNICAL MEMORANDUM

NASA TM X-2034

32047

NASA TM X-2034

FACILITY FORM 602

N70-32047 (ACCESSION NUMBER)

(THRU)

68 (PAGES)

1 (CODE)

TM-X-2034 (NASA CR OR TMX OR AD NUMBER)

28 (CATEGORY)

PERFORMANCE OF AN AUXILIARY INLET EJECTOR NOZZLE WITH FIXED INLET DOORS AND TRIPLE-HINGE TRAILING-EDGE FLAP

by Albert L. Johns and Fred W. Steffen

Lewis Research Center

Cleveland, Ohio 44135

NATIONAL AERONAUTICS AND SPACE ADMINISTRATION • WASHINGTON, D. C. • JULY 1970

1. Report No. NASA TM X-2034	2. Government Accession No.	3. Recipient's Catalog No.
4. Title and Subtitle PERFORMANCE OF AN AUXILIARY INLET EJECTOR NOZZLE WITH FIXED INLET DOORS AND TRIPLE-HINGE TRAILING-EDGE FLAP		5. Report Date July 1970 6. Performing Organization Code
7. Author(s) Albert L. Johns and Fred W. Steffen		8. Performing Organization Report No. E-5497
9. Performing Organization Name and Address Lewis Research Center National Aeronautics and Space Administration Cleveland, Ohio 44135		10. Work Unit No. 720-03 11. Contract or Grant No. 13. Type of Report and Period Covered Technical Memorandum
12. Sponsoring Agency Name and Address National Aeronautics and Space Administration Washington, D.C. 20546		14. Sponsoring Agency Code

15. Supplementary Notes

16. Abstract

An auxiliary inlet ejector nozzle appropriate for a supersonic-cruise aircraft was evaluated over a range of free-stream Mach numbers from 0 to 1.20. Two primary throat areas were used: one to simulate nonreheat operation, and the other for reheat operation. The shroud was fixed in a closed position for subsonic operation. The projected boattail area was 47 percent of the simulated nacelle area. Variation in auxiliary inlets included door type (single and double hinge) and values of tertiary flow area (controlled with fixed-position doors) from 0 to 71.5 percent of the shroud exit area. During subsonic cruise and dry acceleration, the maximum nozzle efficiency was obtained with the double-hinge door configuration. At the reheat power settings, the maximum nozzle efficiency was obtained with the doors closed at Mach 0.60 and higher.

17. Key Words (Suggested by Author(s))	18. Distribution Statement
Propulsion Nozzle	Unclassified - unlimited

19. Security Classif. (of this report)	20. Security Classif. (of this page)	21. No. of Pages	22. Price*
Unclassified	Unclassified	68	$3.00

*For sale by the Clearinghouse for Federal Scientific and Technical Information
Springfield, Virginia 22151

PRECEDING PAGE BLANK NOT FILMED

CONTENTS

PERFORMANCE OF AN AUXILIARY INLET EJECTOR NOZZLE WTH FIXED INLET DOORS AND TRIPLE-HINGE TRAILING-EDGE FLAP

by Albert L. Johns and Fred W. Steffen

Lewis Research Center

SUMMARY

An auxiliary inlet ejector nozzle appropriate for a supersonic-cruise aircraft was tested in the Lewis Research Center's 8- by 6-Foot Supersonic Wind Tunnel to determine the preformance characteristics over a range of free-stream Mach numbers from 0 to 1.20. Room-temperature air was used as the primary and secondary fluid. Two different primary throat areas were used: one to simulate nonreheat operation, and the other for reheat operation.

The secondary shroud represented a fully closed triple-hinge flap which was fixed in a closed position for subsonic operation. The projected boattail area was 47 percent of the simulated nacelle area. Variation in auxiliary inlets included door type (single and double hinge) and values of tertiary flow area from 0 to 71.5 percent of the shroud exit area.

The following results were obtained for a specified pressure ratio schedule that is typical for an afterburning turbojet engine with 4-percent corrected secondary weight flow. The optimum nozzle efficiency was produced by the 10°-20° double-hinge door configuration at subsonic-cruise and dry acceleration power settings. At Mach 0.90, nozzle efficiencies of 0.917 and 0.952 were obtained with the double-hinge door configuration at subsonic cruise and dry acceleration, respectively. Compared to the double-hinge configuration at Mach 0.90, the optimum nozzle efficiencies obtained with the single-hinge doors were 1.5 and 0.8 percent lower at subsonic cruise and dry acceleration, respectively. At takeoff with reheat, a peak nozzle efficiency of 0.992 was obtained with the 16° door configuration. Above Mach 0.60 with reheat the optimum nozzle efficiency was obtained with the doors closed.

INTRODUCTION

As part of an comprehensive program in airbreathing propulsion, the Lewis Research Center is evaluating various exhaust nozzle designs which are appropriate for supersonic-cruise aircraft. Ideally, these nozzle would operate efficiently over a wide range of flight conditions and engine-power settings. Requirements such as these usually necessitate extensive variation in ejector nozzle geometry, including both the primary nozzle and shroud exit areas. The performance of a variable-flap ejector and a low-angle plug nozzle designed for a supersonic-cruise aircraft is reported in references 1 and 2. Another nozzle type of interest is the auxiliary inlet ejector (ref. 3). At low power settings, the auxiliary inlets open to admit tertiary air to prevent overexpansion of the primary jet. Hence, there is a reduced requirement for exit-area variation and a corresponding reduction in boattail angle and projected area.

This report documents the aerodynamic performance of an auxiliary inlet ejector with a triple-hinge trailing-edge flap fixed in a subsonic position. Some of the results will be compared with the installed performance of the same nozzle during flight tests using an F-106B aircraft (ref. 4). For these tests, nacelles that house an afterburning J85-GE-13 turbojet engine as a gas generator were installed under the delta wing of the F-106B with the nozzles extending downstream of the wing trailing edge. The primary nozzle used in this test simulated the General Electric J85-GE-13 afterburning turbojet engine used in the F-106B tests.

The model had a diameter of 8.5 inches (21.59 cm) and was tested in the Lewis Research Center's 8- by 6-Foot Supersonic Wind Tunnel at free-stream Mach numbers from 0 to 1.20 and over a range of nozzle pressure ratios from 1.9 to 9.0. Secondary weight flow was varied from 0 to 16 percent of the primary nozzle weight flow. The configurations were tested at power settings representing subsonic cruise, dry acceleration, and maximum reheat acceleration. Dry air at room temperature was used for both primary and secondary weight flows.

APPARATUS AND PROCEDURE

Installation in Wind Tunnel

A schematic view of the model support system in the 8- by 6-Foot Supersonic Wind Tunnel showing the internal geometry and thrust-measuring system is presented in figure 1. Symbols are defined in appendix A. The grounded portion of the model was supported from the tunnel ceiling by a vertical strut. The floating portion was attached to the primary and secondary air bottles which were cantilevered by flow tubes from ex-

ternal supply manifolds. The primary air bottle was supported by front and rear bearings. The secondary air passed through an annulus around the primary nozzle. The axial force of the nozzle, which included secondary and tertiary flow effects, was transmitted to the load cell located in the nose of the model. Since the floating portion of the model included the afterbody and boattail, the measured force was that resulting from the interaction of the internal and external flows. The wind tunnel installation effects on an isolated 8.5-inch (21.59-cm) afterbody mounted on this jet-exit model are described in reference 5. The static-pressure environment on the 8.5-inch (21.59-cm) jet-exit model immediately upstream of the nozzle-adapter interface is presented in appendix B.

Force Measurements

The primary flow was calculated from a known flow coefficient C_{D8}. The secondary-flow rate was measured by means of a standard ASME flowmetering orifice located in the external supply line. Thrust-minus-drag measurements were obtained from a load-cell readout of the axial forces acting on the floating portion of the model. Internal tare forces determined by internal areas, and measured tare pressures located as shown in figure 1, were accounted for in the thrust calculation.

A static calibration of the thrust-measuring system was obtained by applying known forces to the nozzle and measuring the output of the load cell. A water-cooled jacket surrounded the load cell and maintained a constant temperature of 90° F to eliminate errors in the calibration caused by variations in temperature from aerodynamic heating.

The only external friction drag charged to the nozzle is that downstream of model station 122.84 inches (312 cm, fig. 1). That force acting on the portion of the nozzle between model stations 93.65 inches (238 cm) and 122.84 inches (312 cm) was measured on the load cell; however, it is not considered to be part of the nozzle drag. Its magnitude was estimated by using the semiempirical flat-plate mean skin friction coefficient given in figure 7 of reference 6 as a function of free-stream Mach number and Reynolds number. Previous measurements of the boundary-layer characteristics at the aft end of the jet-exit model in the 8- by 6-Foot Supersonic Wind Tunnel (ref. 7) indicated that the profile and thickness were essentially the same as that computed for a flat plate of equal length. The strut wake appeared to affect only a localized region near the top of the model and resulted in a slightly lower local free-stream velocity than measured on the side and bottom of the model. Therefore, the results of reference 6 were used without correction for three-dimensional flow effects or strut interference effects.

The ideal jet thrust for both the primary and secondary flow was calculated from the measured mass-flow rate expanded from its measured total pressure (P_7 and P_s, respectively) to p_0. Provision was made to set the ideal thrust of the secondary flow

to zero if the total pressure was less than p_0. Review of the data showed that this situation did occur. Hence, tailed data are used to designate such results. Nozzle efficiency is defined as the ratio of the measured thrust minus drag to the ideal thrust of the primary and secondary:

$$\text{Nozzle efficiency} = \frac{F - D}{F_{i,p} + F_{i,s}}$$

In addition to the nozzle efficiency, the data are also presented (appendix C) in the form of nozzle gross-thrust coefficient $(F - D)/F_{i,p}$.

Nozzle Configurations

To provide a comparison with the F-106B flight tests utilizing underwing nacelles housing a J85-GE-13 engine, a J85-GE-13 primary nozzle was simulated for this test. Two different primary throat areas were used (fig. 2). The small throat area simulated nonreheat operation (with a flow coefficient C_{D8} of 0.977), while the large throat area simulated reheat operation (with a flow coefficient C_{D8} of 0.985). The actuating mechanism blockage was simulated by a ring containing 12 slots. Secondary air was diverted through these slots by means of a deflector to simulate primary flap cooling air.

Figure 3 shows details of the triple-hinge trailing-edge flap and some pertinent parameters. The projected boattail area A_β is 47 percent of the simulated nacelle area A_{max} with a boattail angle of 15°. The flap length ratio L/d_8 varied from 2.16 with the smallest throat area to 1.91 with the largest throat area. The fixed flap section used during this test represented a fully closed subsonic-cruise position. An analysis of the trailing-edge flap moments is given in appendix E.

Details of the auxiliary inlets and pertinent parameters are shown in figure 4(a). Two types of auxiliary inlet were tested (single and double hinge) along with a closed auxiliary inlet configuration. The door hinge location is given in table I. In each open auxiliary inlet configuration, the 16 doors were simulated by a continuous ring with 16 equally spaced ribs welded to the upstream side (fig. 4(b)). The closed-door configuration did not have ribs. The single-hinge configurations consisted of 20°, 16°, and 10° door positions, while the double-hinge auxiliary inlets were composed of 10°-20°, 8°-16°, and 5°-10° door configurations.

TABLE I. - DOOR HINGE LOCATION

Door position	Door hinge location							
	Upstream door				Downstream door			
	Length, $L_{\delta 1}$		Diameter, $d_{\delta 1}$		Length, $L_{\delta 2}$		Diameter, $d_{\delta 2}$	
	in.	cm	in.	cm	in.	cm	in.	cm
10^{o}-20^{o}	2.396	6.085	8.26	20.98	7.48	18.99	4.25	10.79
8^{o}-16^{o}	2.447	6.215	8.23	20.90	7.54	19.14	4.28	10.86
5^{o}-10^{o}	2.553	6.485	8.13	20.64	7.82	19.85	4.32	10.96
20^{o}	3.293	8.365	7.85	19.94	----	-----	----	-----
16^{o}	3.293	8.365	7.85	19.94	----	-----	----	-----
10^{o}	3.293	8.365	7.85	19.94	----	-----	----	-----
Closed[a]	-----	-----	----	-----	----	-----	----	-----

[a]Hinge location simulated each door position.

Nozzle Instrumentation

The auxiliary inlet instrumentation is shown in figure 4(b). An internal row of static-pressure orifices was located on door 1 at a meridian angle of 0^{o} and externally on door 8 at a meridian angle of 167.5^{o}. The axial locations x of the door static-pressure orifices are given in table II. The auxiliary inlet ejector instrumentation layout is shown in figure 5. The primary, secondary, and tertiary total pressures were obtained from total-pressure probes, as shown in figures 5(a) and (b). The radial and circumferential locations of the total-pressure probes are given in table III. A row of static-pressure orifices was located at a meridian angle of 90^{o} along the flap internal surface and at 180^{o} along the external boattail. The axial locations x of the static-pressure orifices are given in table IV.

Primary total-pressure profiles of the flow approaching the primary nozzle are shown in figure 6. As expected, the profiles were relatively flat. The nozzle inlet total pressure P_7 was obtained by integrating the pressure across an area-weighted rake located in the primary-flow passage (station 7). The flow is assumed to be circumferentially uniform.

Procedure

Nozzle performance was obtained over a range of free-stream Mach numbers and nozzle pressure ratios. For several of the figures, results are presented with the

TABLE II. - DOOR STATIC-PRESSURE

ORIFICE LOCATIONS

Door position	Internal; circumferential position, $\theta = 0^{\circ}$			External; circumferential position, $\theta = 167.5^{\circ}$		
	Tap	Axial distance, x		Tap	Axial distance, x	
		in.	cm		in.	cm
10°-20°	1	-6.77	-17.20	1	-7.19	-18.26
	2	-6.04	-15.34	2	-6.69	-17.00
	3	-5.44	-13.81	3	-6.04	-15.34
	4	-4.70	-11.94	4	-5.35	-13.59
	5	-3.87	-9.83	5	-4.71	-11.79
	6	-3.27	-8.30	6	-4.10	-10.42
				7	-3.43	-8.72
8°-16°	1	-6.81	-17.29	1	-7.16	-18.18
	2	-6.12	-15.54	2	-6.68	-16.98
	3	-5.46	-13.86	3	-6.02	-15.30
	4	-4.48	-11.39	4	-5.34	-13.56
	5	-3.64	-9.25	5	-4.68	-11.90
	6	-3.26	-8.27	6	-3.99	-10.14
				7	-3.38	-8.58
5°-10°	1	-6.60	-16.75	1	-7.08	-17.99
	2	-6.02	-15.29	2	-6.68	-16.96
	3	-5.41	-13.73	3	-6.00	-15.25
	4	-4.70	-11.93	4	-5.33	-13.54
	5	-4.00	-10.16	5	-4.66	-11.83
	6	-3.32	-8.42	6	-3.99	-10.14
				7	-3.32	-8.42
20°	1	-5.97	-15.17	1	-6.30	-16.00
	2	-5.39	-13.70	2	-5.75	-14.60
	3	-4.65	-11.82	3	-5.31	-13.49
	4	-4.08	-10.35	4	-4.86	-12.34
	5	-3.66	-9.31	5	-4.39	-11.14
	6	-3.27	-8.30	6	-4.08	-10.37
				7	-3.36	-8.53
16°	1	-6.00	-15.25	1	-6.17	-15.67
	2	-5.44	-13.81	2	-5.75	-14.61
	3	-4.79	-12.17	3	-5.29	-13.44
	4	-4.15	-10.53	4	-4.82	-12.25
	5	-3.68	-9.34	5	-4.34	-11.01
	6	-3.25	-8.26	6	-3.83	-9.72
				7	-3.30	-8.38
10°	1	-6.13	-15.57	1	-7.54	-19.16
	2	-5.49	-13.94	2	-5.76	-14.62
	3	-4.92	-12.51	3	-5.27	-13.39
	4	-4.37	-11.09	4	-4.78	-12.14
	5	-3.81	-9.67	5	-4.28	-10.87
	6	-3.25	-8.26	6	-3.76	-9.56
				7	-3.24	-8.22
Closed	1	-7.36	-18.70	1	-7.54	-19.15
	2	-6.09	-15.47	2	-7.29	-18.51
	3	-5.13	-13.03	3	-3.52	-8.94
	4	-3.11	-7.90			

TABLE III. - TOTAL-PRESSURE

PROBE LOCATIONS

(a) Open- and closed-door total-pressure rake (Open-door rake at model station 133.86 in. (340 cm); $\theta = 112.5^{\circ}$; door 6. Closed-door rake at station 123.62 in. (314 cm); $\theta = 135^{\circ}$; door 7.)

Probe	Radial distance from secondary shroud external surface, z	
	in.	cm
1	0.125	0.318
2	.500	1.270
3	1.000	2.540
4	1.800	4.572
5	2.750	6.985

(b) Auxiliary-inlet total-pressure rake ($\theta = 225^{\circ}$; door 11)

Probe	Radial distance from secondary shroud internal surface, z'	
	in.	cm
1	0.062	0.158
2	.312	.792
3	.500	1.270
4	.750	1.905
5	1.000	2.540

(c) Primary nozzle secondary total-pressure probes (r = 3.25 in. (8.263 cm))

Probe	Circumferential position, θ, deg
1	0
2	90
3	180
4	270

TABLE IV. - TRAILING FLAP STATIC-

PRESSURE ORIFICE LOCATIONS

Internal			External		
Tap	Axial distance, x		Tap	Axial distance, x	
	in.	cm		in.	cm
1	-2.348	-5.96	1	-1.37	-3.48
2	-1.811	-4.60	2	1.925	4.89
3	-1.146	-2.91	3	2.661	6.76
4	-.396	-1.006	4	3.142	7.98
5	.246	.625	5	3.535	8.98
6	1.402	3.56	6	3.949	10.03
7	2.898	7.36	7	4.362	11.08
8	4.606	11.70	8	4.787	12.16
9	6.102	15.50	9	5.232	13.29
			10	5.689	14.45
			11	6.165	15.66
			12	6.658	16.91

assumption of a nozzle pressure ratio schedule appropriate for a turbojet engine cycle (fig. 7). The nozzle pressure ratio was varied by changing the nozzle inlet total pressure. The maximum pressure ratio at each Mach number was restricted because of the limitations of the primary air supply. Secondary weight flow was varied from 0 to 16 percent of the primary flow. Nozzle performance characteristics at pertinent test conditions are presented in appendix C. However, the following results and discussion pertain to the assumed pressure ratio schedule with a nominal 4-percent corrected secondary weight flow.

RESULTS AND DISCUSSION

Comparison of Optimum Nozzle Efficiencies of Single- and Double-Hinge Doors

A comparison of the optimum nozzle efficiencies of the single- and double-hinge door configurations is shown in figure 8 at the subsonic-cruise and dry-acceleration simulated power settings. The 4-percent corrected secondary weight flow chosen for the subsonic-cruise, dry-, and reheat-acceleration power settings was considered to be typical of the values which might be used for supersonic-cruise vehicles. Data are not presented in figure 8 above takeoff for the reheat power setting because the closed-door

configuration produced the optimum nozzle efficiency. Optimum nozzle efficiency was obtained with double-hinge door configurations at subsonic-cruise and dry-acceleration power settings. For example at Mach 0.90 (subsonic cruise), the optimum nozzle efficiencies are 0.902 and 0.917 for the single- and double-hinge doors, respectively. At the higher nozzle pressure ratios at Mach 0.90 (dry acceleration), optimum nozzle efficiencies of 0.944 and 0.952 were obtained with the single- and double-hinge doors, respectively. With a reheat takeoff, the optimum nozzle efficiencies were 0.992 and 0.983 for the single- and double-hinge doors, respectively.

Single-Hinge Door Performance

The performance and secondary total-pressure recovery requirements of the single-hinge doors are shown in figure 9 as a comparison between the estimated floating position performance and the best measured performance. The data points representing the estimated floating performance are obtained from crossplots. The method used to obtain the estimated floating door position is given in appendix D. The term "best measured nozzle efficiency" is used to indicate the highest nozzle efficiency obtained from the door configurations which were tested at each Mach number. However, untested door positions may have provided higher nozzle efficiencies. The best measured nozzle efficiency was 1/2 to 1 percent higher than the estimated floating efficiency at the subsonic-cruise power setting (fig. 9(a)). At Mach 0.90, nozzle efficiencies of 0.902 and 0.897 were obtained for the best measured and the estimated floating door positions, respectively. The estimated floating door position (angle) was always less than that required for peak efficiency. In either case, the secondary total pressure was low enough that it could be obtained from a free-stream source. At dry-acceleration power setting (fig. 9(b)), the best measured nozzle efficiencies and the associated door positions were both higher than the corresponding floating values. It can also be seen that, in both cases, the required secondary total-pressure recovery was increased significantly by opening the doors from the estimated floating position. This increased secondary pressure is probably indicative of an increased pressure level in the primary base region, which in turn is responsible for the increased performance. A curve of free-stream static-pressure ratio is presented in figure 9(b) for comparison. It is interesting to note that secondary total pressures considerably above p_0 can be obtained by forcing the doors to remain open. These higher pressures are also probably responsible for forcing the floating doors to partly close. At the dry-acceleration power setting (fig. 9(b)), the best measured nozzle efficiency and the door position where it was obtained were both higher than those obtained at the estimate floating position. At takeoff, nozzle efficiency of 0.995 was obtained for the optimum performance. At

Mach 0.90, 0.943 was the best measured nozzle efficiency and 0.928 the estimated floating nozzle efficiency. At takeoff, the 4-percent corrected secondary weight flow could not be obtained from the free stream. With reheat (fig. 9(c)), the estimated floating and optimum nozzle efficiencies were obtained with the inlet doors closed at Mach numbers other than takeoff. At takeoff, a best measured nozzle efficiency of 0.992 was obtained with the 16° door configuration. The fully open door configuration (20°) was not tested with the reheat primary nozzle. However, 4-percent corrected secondary weight flow cannot be obtained from the free stream at several of the Mach numbers. This problem may not be encountered, however, if a variable shroud is used instead of the fixed-position shroud.

The effect of single-hinge door angle on the ratio of boattail drag to ideal gross thrust is presented in figure 10 for the three power settings. The boattail drag was normally reduced as the door opening was increased. For subsonic cruise, the drop in nozzle efficiency between Mach 0.85 and 1.00 seen in figure 9(a) appears to be primarily due to the increased boattail drag shown in figure 10(a). A similar effect is seen for dry acceleration. The boattail drag is less important during dry or reheat acceleration when the primary nozzle ideal thrust is large.

Pressure forces were computed on the inlet doors and on the secondary shroud at subsonic speeds. It is assumed that the flow around and through the model is symmetrical; hence, there was one inlet door instrumented externally at 167.5° and one door internally at 0°. The shroud was instrumented internally at 90° and externally at 180°. These component forces are shown in figure 11 at subsonic cruise for various inlet door angles. The secondary momentum shown in figure 11 was computed with the assumption that the static pressure is constant in the region of the internal surfaces of the doors and the primary nozzle flap surface. The largest component force at the 10° door angle (door position for peak efficiency) was the boattail drag, which was about 4 percent of the ideal primary and secondary thrusts. Inlet doors and the forward shroud surface also provided significant drag components.

The effect of single-hinge door angle on the nozzle efficiency is shown in figure 12. At the subsonic-cruise and dry-acceleration power settings (figs. 12(a) and (b)), the 10° door position generally provided the optimum nozzle efficiency. The results in figure 12(c) indicate that with reheat acceleration, the closed-door configuration produced the best measured nozzle efficiency at Mach numbers from 0.60 to 1.20 where the nozzle is fully expanded or underexpanded. The 16° inlet doors, maximum open doors tested with reheat, provided peak performance at takeoff for this configuration.

The effect of single-hinge door position on door moment coefficient per inch of width is shown in figure 13 for the three power settings. A simple pin connection was assumed in calculating the moments on the single-hinge doors. Door equilibrium is defined in appendix D. During subsonic cruise (fig. 13(a)), the doors would be in equilib-

rium at about 8°. At the dry-acceleration power setting (fig. 13(b)), the door equilibrium position is about 7.5° for Mach 0.60 and 0.70, and the doors would close between Mach 0.85 and 0.90. At the reheat power setting (fig. 13(c)), the inlet door would be open at takeoff and closed at Mach numbers from 0.60 to 1.20.

Figure 14 shows the effect of single-hinge door angle on auxiliary inlet flow velocity profiles at subsonic cruise and dry acceleration. The peak velocity occurred near the shroud surface opposite the inlet door. The peak velocities were generally between 70 and 80 percent of the free-stream velocity at the subsonic-cruise power setting (fig. 14(a)). The flow separated from the door at Mach 1.00 with the 16° and 20° door configurations. Separated flow was also indicated at Mach 0.70 with the 20° doors by the probe nearest the door. At the higher nozzle pressure ratio required for dry acceleration (fig. 14(b)), the peak inlet velocities were reduced to between 60 and 70 percent of the free-stream velocity. The inlet flow generally peaked with the 20° door angle. Separated flow occurred at the dry-acceleration power setting with the 16° doors at most Mach numbers from 0.85 to 1.00. At these conditions, the floating doors would be nearly or fully closed.

The effect of single-hinge door angle on the trailing-edge flap moment coefficient per inch of width is presented in figure 15 for the three power settings. Figure 15(a) shows that at subsonic cruise the trailing-edge flaps would be off the inner stop with the optimum door position (10°) up to Mach 0.95. However, the trailing-edge flaps would be on the inner stop over the dry-acceleration range and at maximum reheat up to Mach 0.90 (figs. 15(b) and (c)). It should be noted that when the trailing-edge flaps are off the inner stop at subsonic cruise, a loss in nozzle efficiency is likely to occur. The analysis of the flap moment calculation is shown in appendix E.

Internal and external static-pressure distributions on the inlet doors and secondary shroud are shown in figure 16 at Mach 0.90 for subsonic cruise and dry acceleration, and at Mach 0 and 0.95 for reheat acceleration. At subsonic cruise (fig. 16(a)), the nozzle is overexpanded internally with the doors closed. The overexpansion was generally eliminated when the tertiary inlets were opened. At the higher pressure ratio for dry acceleration (fig. 16(b)), opening the doors increased the internal nozzle pressures upstream of the shroud throat to values 20 to 25 percent larger than free-stream static. This is indicative of the significant diffusion of the incoming tertiary flow as it enters the nozzle. Optimum performance at this flight condition was obtained with a 10° door angle, but the doors would tend to float to the closed position with a reduction in performance. For a reheat takeoff (fig. 16(c)), opening the inlet doors caused a slight increase in internal pressures and an increase in nozzle efficiency. The doors should be fully open at this flight condition for best efficiency. However, for a reheat acceleration at Mach 0.95 (fig. 16(d)), opening the inlet doors caused a reduction in the

internal pressures and a loss in nozzle efficiency. The doors should be closed at this flight condition for best efficiency.

Double-Hinge Door Performance

The performance of the double-hinge door configurations is presented in figures 17 to 24. The effect of double-hinge doors on the nozzle performance was similar to that obtained with the single-hinge doors, as described in the preceding section. At subsonic cruise (fig. 17(a)), the floating door nozzle efficiency was always less than the peak performance and was obtained at a lower door angle. At Mach 0.90, for example, the floating door nozzle efficiency was 0.884, compared to a peak value of 0.917. The same trends were obtained for a dry acceleration. At Mach 0.90 (fig. 17(b)), the floating doors would be closed and provide an efficiency of 0.926, compared to a peak efficiency of 0.952 with the doors fully open at 10°-20°. Opening the doors again forced the secondary total-pressure requirements to be in excess of free-stream static which is indicative of the doors' ability to raise internal pressures above p_0. This configuration would not provide secondary flow at takeoff. For a reheat acceleration configuration (fig. 17(c)), the optimum nozzle efficiency was obtained with the inlet doors closed at Mach numbers from 0.60 to 1.20. For this Mach number range, it was estimated that the inlet doors would float to the closed position and provide peak nozzle efficiency. The inlet doors should be fully open to provide peak performance at takeoff. However, the 8°-16° inlet doors were the maximum open position tested with reheat. The nozzle pumping characteristics are poor for the reheat configuration at all Mach numbers from takeoff to Mach 1.2.

The effect of double-hinge door angle on boattail drag is shown in figure 18 for three power settings. Boattail drag was most sensitive to door angle at the subsonic-cruise conditions (fig. 18(a)), particularly at Mach numbers 0.70 and 0.85 where increased opening of the inlets decreased the boattail drag. At Mach 0.90, the boattail drag was about 4 percent of the ideal thrust. At the higher power settings for acceleration (figs. 18(b) and (c)), the boattail drag was a smaller percent of the nozzle ideal thrust since the primary thrust was larger. Door angle had little effect on boattail drag at these flight conditions. In general, however, the boattail drag tended to decrease as door opening increased. For subsonic cruise, the drop in nozzle efficiency between Mach 0.85 and 1.00 (seen in fig. 17(a)) appears to be primarily due to the increased boattail drag shown in figure 18(a). A similar effect is seen for dry acceleration.

An analysis of the pressure forces on the inlet doors and the secondary shroud was made at the subsonic-cruise Mach number, 0.90. These component forces are shown in figure 19 for various inlet door angles. The secondary momentum shown in figure 19

was computed with the assumption that the static pressure is constant in the region of the door internal surfaces and the primary nozzle flap surfaces. The largest component force at the estimated floating position (4.75°-9.5°) was the boattail drag, which was about 4 percent of the ideal gross thrust. However, at the inlet position (10°-20°) where peak efficiency was obtained, large drag forces of 4 and 5.8 percent of the ideal gross thrust were measured on the boattail and internal secondary shroud upstream surfaces, respectively. There also was a large drag force of about 4.6 percent measured on the internal surfaces of the upstream doors. These drag forces were offset, however, by thrust forces.

The effect of double-hinge door angle on the nozzle efficiency is presented in figure 20 for the three power settings. The best measured nozzle efficiency was generally obtained with the 10°-20° door configuration at subsonic cruise and dry acceleration (figs. 20(a) and (b)). With reheat acceleration (fig. 20(c)), the closed-door configuration produced the optimum nozzle efficiency at Mach numbers from 0.60 to 1.20. The 8°-16° inlet doors provided peak performance at takeoff for this configuration; however, the fully open (10°-20°) inlet door configuration was not tested at reheat acceleration. It should be noted that the internal expansion pressure ratio for the reheat configuration is 5.57. Hence, the nozzle is underexpanded above Mach 0.95 for the power setting used since the shroud was fixed in the closed position.

In order to obtain the door hinge moments about the first hinge of the double-hinge doors, the fixed doors were assumed to have the mechanism shown in appendix D. The results in figure 21(a) indicate that the doors would be open at about a 5°-10° angle over the subsonic-cruise power setting Mach number range. However, with dry acceleration (fig. 21(b)), the doors would be open from takeoff up to Mach 0.85 and closed (if free floating) at Mach numbers from 0.85 to 1.00. At the reheat power setting (fig. 21(c)), the door moment coefficient indicates that the inlet doors would be open at takeoff and closed at Mach numbers from 0.60 to 1.20.

The effect of double-hinge door angle on the auxiliary-inlet flow velocity profiles at subsonic cruise and dry acceleration is presented in figure 22. The reheat configurations indicated separated flow at all Mach numbers; hence, no data are shown. The peak inlet velocities (fig. 22(a)) were generally between 70 and 80 percent of the free-stream velocity V_0. These peak velocities occurred along the secondary shroud leading edge. At the subsonic-cruise power setting (fig. 22(a)), separated flow occurred with the 10°-20° door configuration from Mach numbers of 0.85 to 0.95. At the higher pressure ratios required for dry acceleration (fig. 22(b)), the peak velocities were reduced, particularly at Mach numbers of 0.95 and 1.00. At these conditions, floating inlet doors would be closed. The inlet flow generally peaked with the 5°-10° door angle.

The effect of double-hinge door angle on the trailing-edge flap moment coefficient per inch of width is shown in figure 23 for the three power settings over the Mach

number range tested. The analysis of the flap moment calculation is shown in appendix E. At subsonic cruise (fig. 23(a)), the trailing-edge flaps would be off the inner stop with optimum door position (10°-20°) up to Mach 0.95. However, the trailing-edge flaps would be on the inner stop over the dry-acceleration range and at maximum reheat up to Mach 0.90 (figs. 23(b) and (c)).

Internal and external static-pressure distributions of the auxiliary inlet door and secondary shroud are shown in figure 24 at Mach 0.90 for subsonic cruise and dry acceleration, and at Mach 0 and 0.95 for reheat acceleration. At subsonic cruise (fig. 24(a)), the nozzle is overexpanded internally with the doors closed. The overexpansion was generally eliminated when the tertiary inlets were opened. At the higher nozzle pressure ratio for dry acceleration (fig. 24(b)), there was some increase in internal pressure to above p_0 when the doors were opened. Peak efficiency at this flight condition was obtained with the fully open inlet doors, but the doors would tend to float to the closed position, producing a loss in performance. For a reheat power setting (fig. 24(c)), opening the inlet doors at takeoff caused a slight increase in internal pressures and an increase in nozzle efficiency. The doors should be fully open at this flight condition for best efficiency. However, at Mach 0.95 (fig. 24(d)), opening the inlet doors caused a reduction in internal pressures and a loss in nozzle efficiency. The doors should be closed at this flight condition for best efficiency.

Model Boundary-Layer Characteristics

The boundary-layer characteristics have been measured previously on this jet-exit model over a range of free-stream Mach numbers from 0.56 to 1.46 and are presented and discussed in reference 7. These measurements indicated a well-developed turbulent profile with an average momentum-thickness-to-model-diameter ratio of 0.019 for the Mach number range of this report. A single rake measurement was made during the current test with the inlet doors closed, and the resulting boundary-layer profiles are shown in figure 25 for two power settings. Also shown for the same conditions is a boundary-layer profile downstream of the fully open inlet doors (20° single and 10°-20° double hinge). Figure 25(a) shows the comparison at the subsonic-cruise power setting. Opening the inlet doors resulted in a slight decrease in the local stream velocity at Mach numbers from 0.90 to 1.00. For the dry-acceleration configuration (fig. 25(b)), there was a general increase in local stream velocity at Mach numbers from 0.85 to 1.00. For these conditions, the inlet doors provide little flow, as was shown in figure 22(b). There was even some evidence of separated flow at these higher pressure ratios for dry acceleration.

SUMMARY OF RESULTS

An experimental investigation was conducted to determine the performance characteristics of an auxiliary-inlet ejector nozzle that is appropriate for a supersonic-cruise aircraft. The nozzle performance was obtained over a range of free-stream Mach numbers from 0 to 1.20. Corrected secondary weight flow of 4 percent of the primary nozzle weight flow was investigated. Two different primary throat areas were used: one to simulate nonreheat operation (subsonic cruise and dry acceleration), and the other for reheat operation. The auxiliary inlet configuration consisted of fixed-position single-hinge doors (10°, 16°, and 20°), double-hinge doors (5°-10°, 8°-16°, and 10°-20°), and closed doors which provided a tertiary flow area variation from 0 to 71.5 percent of the shroud exit area. The secondary shroud was a triple-hinge flap which was fixed in a closed position with a boattail angle of 15°. Its projected boattail area was 47 percent of the simulated nacelle area. The following results were obtained for a specified pressure ratio schedule that is typical for an afterburning turbojet engine:

Subsonic cruise:

1. The double-hinge doors provided higher nozzle efficiency than the single-hinge doors. For example, at Mach 0.9 the best measured nozzle efficiency of the double doors was 0.916, compared to 0.901 for the single doors.

2. Boattail drag was a function of door position and varied from 0.30 percent of the ideal gross thrust at Mach 0.7 to 11.25 percent at Mach 1.0.

3. The equilibrium door angle was less than that required for peak nozzle efficiency. With single-hinge doors, the estimated floating performance was near the peak value. However, with double-hinge doors, the estimated floating performance was as much as 3.1 percent lower than the best measured preformance.

4. Pumping characteristics were adequate to provide 4-percent corrected secondary flow from a free-stream source.

5. In general, the trailing-edge flap moment coefficient indicated an opening moment for most door positions up to Mach 0.90.

6. Opening the inlet doors increased the internal pressure significantly above free-stream static pressure.

7. Peak inlet velocities were generally between 70 and 80 percent of free-stream velocity. Separated flow was measured with the full-open door configurations at Mach numbers of 0.85 and greater.

Dry acceleration:

1. In general, the double-hinge doors provided higher nozzle efficiency than the single-hinge doors.

2. Boattail drag varied from 1/2 percent of the ideal gross thrust at Mach 0.7 to $6\frac{1}{4}$ percent at Mach 1.0.

3. The equilibrium door angle was less than that required for peak nozzle efficiency. With single doors above Mach 0.6, the floating performance was near the peak value. However, with double-hinge doors, the estimated floating value was generally 1 to $2\frac{1}{2}$ percent lower than the peak value.

4. Pumping characteristics were adequate to provide 4-percent corrected secondary flow from a free-stream source at all Mach numbers except takeoff.

5. Trailing-edge flap moment coefficient indicated a closing moment for the fixed position tested.

6. Peak inlet velocities were generally between 60 and 70 percent of free-stream velocity. Separated flow was measured for some door positions at Mach numbers of 0.85 and greater.

7. Opening the inlet doors increased the internal pressure significantly above free-stream static pressure.

Reheat acceleration:

1. At subsonic and transonic speeds, best measured nozzle efficiency was obtained with the doors closed, particularly at Mach numbers from 0.60 to 1.20 where the nozzle was underexpanded.

2. Boattail drag was unimportant at Mach numbers up to 0.85 and had a value of 3.8 percent of the ideal gross thrust at Mach 1.20.

3. Pumping characteristics were generally too poor at all Mach numbers to supply 4-percent corrected secondary flow from a free-stream source.

4. Trailing-edge flap moment coefficient indicated an opening moment above Mach numbers of 0.90.

Lewis Research Center,
National Aeronautics and Space Administration,
Cleveland, Ohio, February 5, 1970,
720-03.

APPENDIX A

SYMBOLS

A	area (projected)
AR	aspect ratio (width/length)
A_{max}	simulated nacelle area
A_{ter}	door tertiary flow area normal to external door tip
C_{D8}	nozzle flow coefficient, w_p/w_i
C_m	moment coefficient, $\left(\sum m_{ext} - \sum m_{int}\right)/(A_{max})(d_{max})(P_7)$
D	drag
d	diameter
d_{max}	model diameter (equivalent to nacelle diameter)
d_s	minimum diameter of secondary shroud
F	thrust
$F_1, \ldots, F_4$	forces acting on door
L	length
l	length of secondary shroud, 9.842 in. (25.00 cm)
M	Mach number
m	moment
m_{TR}	reaction moment
P	total pressure
p	static pressure
R	total radius
r	radius from center to local probe
s	axial distance from primary nozzle exit to minimum secondary shroud diameter
T	total temperature
V	velocity
w	weight-flow rate

x	axial distance measured from minimum secondary shroud diameter
z	radial distance from secondary shroud external surface
z'	radial distance from secondary shroud internal surface
α	primary nozzle flap angle
β	boattail angle
δ	door angle
θ	circumferential position, deg
$\omega\sqrt{\tau}$	corrected secondary-weight-flow-rate ratio, $(w_s/w_p)\sqrt{T_s/T_p}$

Subscripts:

d	door
ext	external
f	flap
i	ideal
int	internal
p	primary
s	secondary
ter	tertiary
x	condition at distance x
β	boattail
0	free stream
1	upstream door
2	downstream door
7	nozzle inlet
8	nozzle throat
9	nozzle exit

APPENDIX B

STATIC-PRESSURE ENVIRONMENT ON 8.5-INCH (21.59-CM) JET-EXIT MODEL IMMEDIATELY UPSTREAM OF NOZZLE-ADAPTER INTERFACE

There has been some indication from recent jet-exit programs that the local static pressure on the 8.5-inch (21.59-cm) adapter ahead of the nozzle was somewhat lower than p_0, particularly at subsonic-cruise Mach numbers of 0.85 and 0.90. These static-pressure measurements were rather limited; that is, the instrumentation generally consisted of a single row of static-pressure orifices on the bottom of the model (180° from the support strut). These measurements usually only extended upstream a few model diameters from the end of the nozzle, and at subsonic speeds would be influenced by the nozzle boattail. It is, therefore, risky to comment on the general quality of the local flow field based on this limited amount of information.

Additional measurements were subsequently made to better define the static-pressure environment that exists on the 8.5-inch (21.59-cm) jet-exit model at subsonic speeds, just ahead of the nozzle-adapter interface. Previous measurements had indicated that there was no loss in total pressure at the aft end of this model at subsonic speeds, except for a localized region at the top of the model in the wake of the strut. Therefore, a model static-pressure deviation from p_0 can be used to indicate a local flow velocity that is different from the free-stream value.

A sketch of the model and the location of the static-pressure instrumentation used is shown on figure 26. A cylindrical afterbody was attached to the model adapter to represent a typical exhaust-nozzle installation. A total of 20 static-pressure measurements was made at the three axial stations shown - 2.0, 2.5, and 3.0 model diameters from the end of the cylindrical afterbody.

The model was tested at several subsonic speeds from Mach numbers of 0.61 to 0.96. The model static pressures were ratioed to the computed free-stream value of p_0, and the results are shown on figure 27. At station 3 the measured static pressures had a maximum circumferential distortion of about 1 percent. The average static pressure at this station was within 1/4 percent of the free-stream value. At station 2 there was very little circumferential distortion, and the average static pressure was generally within 1/2 percent of p_0. The dashed line is used to connect an average of the measured static pressures at each of the three axial stations. The slight tail-off in static pressure from station 3 to station 2 probably resulted from the effect of the base feeding forward on the model.

Based on the results presented on figure 27, it is concluded that the local flow at the aft end of the 8.5-inch (21.59-cm) jet-exit model is essentially at free-stream conditions. It is, therefore, recommended that nozzle performance continue to be referenced to free-stream conditions, as has been done during the past several years.

APPENDIX C

NOZZLE PERFORMANCE CHARACTERISTICS

The nozzle gross-thrust coefficient and pumping characteristics obtained during the test are presented for each auxiliary-inlet door configuration: first, for primary nozzle configuration I ($A_9/A_8 = 1.99$); and second, for primary nozzle configuration II ($A_9/A_8 = 1.42$). Data are presented as a function of nozzle pressure ratio and corrected secondary-weight-flow ratio for a range of free-stream Mach number in figures 28 to 31.

APPENDIX D

AUXILIARY INLET DOOR HINGE MOMENT ANALYSIS

For single-hinge doors, the hinge moment was obtained simply by integrating the moment of the internal and external pressure distributions. To obtain the hinge moment about the front hinge of a double-hinge door, the fixed door was assumed to have the mechanism shown in figure 32. This mechanism, with $l_4 \sim 2l_6$ would give a door-angle ratio δ_2/δ_1 of approximately 2.0.

The equations to determine the total hinge moment at z are as follows. If the rear door is considered to be a free body in equilibrium, the sum of the forces and moments about x would be equal to 0.

$$F_1 l_1 - F_2 l_2 = 0 \tag{D1}$$

$$F_1 \sin \delta_2 + F_2 \sin \varphi_2 - F_3 \sin \varphi_3 = 0 \tag{D2}$$

$$F_1 \cos \delta_2 + F_2 \cos \varphi_2 - F_3 \cos \varphi_3 = 0 \tag{D3}$$

In these equations, F_3 is considered as the equilibrant; δ_2, φ_2, and l_2 are known constants for any particular door setting; F_1 and l_1 are determined from measured pressure distributions on the rear door; F_2 is the reaction of the part against the side of the slot and must be normal to the side of the slot; F_2, φ_3, and F_3 can be determined from the solution of equation (D1) and the simultaneous solution of equations (D2) and (D3).

$$F_2 = \frac{F_1 l_1}{l_2} \tag{D4}$$

$$\varphi_3 = \tan^{-1} \frac{F_1 \sin \delta_2 + F_2 \sin \varphi_2}{F_1 \cos \delta_2 + F_2 \cos \varphi_2} \tag{D5}$$

$$F_3 = \frac{F_1 \sin \delta_2 + F_2 \sin \varphi_2}{\sin \varphi_3} \tag{D6}$$

Then the moment about Z caused by the forces on the rear door is

$$m_{F\text{-}R} = F_3 l_3 = F_3 l_4 \cos \varphi_3 = F_3 l_4 \cos(\varphi_3 - \delta_1) \tag{D7}$$

where F_3 is the resultant of F_1 and F_2, and δ_1 and l_4 are known constants for any particular door setting. The total moment about Z is then

$$m_Z = m_{F\text{-}R} + F_4 l_5 \tag{D8}$$

where F_4 and l_5 are obtained from measured pressure distribution on the front door.

For both single- and double-hinge door configurations, door equilibrium is defined as (1) that door angle where the moment curve passes through zero moment with a negative line-slope, or (2) the condition where moments on the closed doors are negative $p_{int} < p_{ext}$. At the latter condition, the doors are on the "outer stop" and, hence, in equilibrium.

APPENDIX E

ANALYSIS OF FLAP MOMENTS

A schematic sectional view of a triple-hinge flap and the forces acting upon it is shown in figure 33. Four hinge points allow the flap to move as a four-bar linkage. Aerodynamic forces F_{FB} and F_{SB} act on the outer and inner surfaces of the boattail (T-S). Aerodynamic forces F_{JS} and F_{SS} act on the outer and inner surfaces of the nozzle wall (P-S). It is assumed that no aerodynamic forces act on the link P-Q.

The fixed model used to obtain the data in this report simulated a fully closed position of an aerodynamically positioned triple-hinge flap. In this position, a stop would supply a reaction moment $-m_{TR}$ about point T, to prevent the flap from closing further. If the forces (as obtained from measured pressures) acting on the fixed model required m_{TR} to be negative or zero, the position of the fixed geometry would properly simulate the position of the assumed movable geometry. The equations and assumptions used to relate the measured pressures to the required reaction moment m_{TR} are presented in the following paragraphs.

If a reaction moment exists at point T, and is of sufficient magnitude to maintain the linkage in equilibrium, the linkage becomes a rigid body. The summation of moments about T can then be written as

$$F_Q\, d_{FQT} + F_{JS}\, d_{FJS} + F_{FB}\, d_{FFBT} + F_{SS}\, d_{FSST} - F_{SB}\, d_{FSBT} + m_{TR} = 0 \qquad \text{(E1)}$$

Note that F_Q must be alined with the link P-Q since Q is a hinge point.

Another equation that can be written is the summation of moments about point S caused by the forces acting on the nozzle wall. This summation must also equal zero since S is a hinge point.

$$F_Q\, d_{FQS} - F_{SS}\, d_{FSSS} + F_{JS}\, d_{FISS} = 0 \qquad \text{(E2)}$$

Solving equation (E2) for F_Q yields

$$F_Q = F_{SS}\frac{d_{FSSS}}{d_{FQS}} - F_{JS}\frac{F_{FJSS}}{d_{FQS}} \qquad \text{(E2a)}$$

Substituting equation (E2a) into equation (E1) and solving for m_{TR} yield

$$m_{TR} = F_{JS} \frac{d_{FJSS}}{d_{FQS}} d_{FQT} - d_{FJST} - F_{SS} \frac{d_{FSSS}}{d_{FQS}} d_{FQT} + d_{FSST}$$

$$-F_{FB}\, d_{FFBT} + F_{SB}\, d_{FSBT} \qquad \text{(E3)}$$

Forces acting in the cavity between the boattail and nozzle surface were obtained by assuming that a uniform pressure acts in this region:

$$F_{SS} = P_s A_\beta \qquad \text{(E4)}$$

and

$$F_{SB} = P_s A_B \qquad \text{(E5)}$$

where A_β and A_B are the inner surface area of the boattail and the outer surface of the nozzle wall, respectively, and P_s was assumed to be the secondary total pressure.

The inner nozzle wall forces and boattail forces were obtained from pressure integrations:

$$F_{JS} = \int p_J \, dA \qquad \text{(Nozzle wall)} \qquad \text{(E6)}$$

and

$$F_{FB} = \int p_F \, dA \qquad \text{(Boattail)} \qquad \text{(E7)}$$

The dimensions d_{FQS}, d_{FQT}, d_{FSSS}, d_{FSST}, d_{FSBT}, and K_{ST} are constants obtained from the fixed model geometry. Other dimensions were obtained as follows:

$$d_{FJSS} = \frac{\int p_J l \, dl}{\int p_J \, dl} \qquad \text{(Nozzle wall)}$$

$$d_{FJST} = d_{FJSS} - K_{ST}$$

and

$$d_{FFBT} = \frac{\int p_F l \, dl}{\int p_F \, dl} \qquad \text{(Boattail)}$$

REFERENCES

1. Steffen, Fred W.; and Jones, John R.: Performance of a Wind Tunnel Model of an Aerodynamically Positioned Variable Flap Ejector at Mach Numbers From 0 to 2.0. NASA TM X-1639, 1968.

2. Bresnahan, Donald L.: Experimental Investigation of a 10^{o} Conical Turbojet Plug Nozzle With Iris Primary and Translating Shroud at Mach Numbers From 0 to 2.0. NASA TM X-1709, 1968.

3. Shrewsbury, George D.; and Jones, John R.: Static Performance of an Auxiliary Inlet Ejector Nozzle for Supersonic-Cruise Aircraft. NASA TM X-1653, 1968.

4. Crabs, Clifford C.; Mikkelson, Daniel C.; and Boyer, Earle O.: An Inflight Investigation of Airframe Effects on Propulsion System Performance at Transonic Speeds. Presented at the 13th Annual Symposium of the Society of Experimental Test Pilots, Los Angeles, Calif., Sept. 25-27, 1969.

5. Blaha, Bernard J.; and Bresnahan, Donald L.: Wind Tunnel Installation Effects on Isolated Afterbodies at Mach Numbers From 0.56 to 1.5. NASA TM X-52581, 1969.

6. Smith, K. G.: Methods and Charts for Estimating Skin Friction Drag in Wind Tunnel Test With Zero Heat Transfer. Rep. ARC-CP-824, Aeronautical Research Council, 1965.

7. Harrington, Douglas E.: Jet Effects on Boattail Pressure Drag of Isolated Ejector Nozzles at Mach Numbers From 0.60 to 1.47. NASA TM X-1785, 1969.

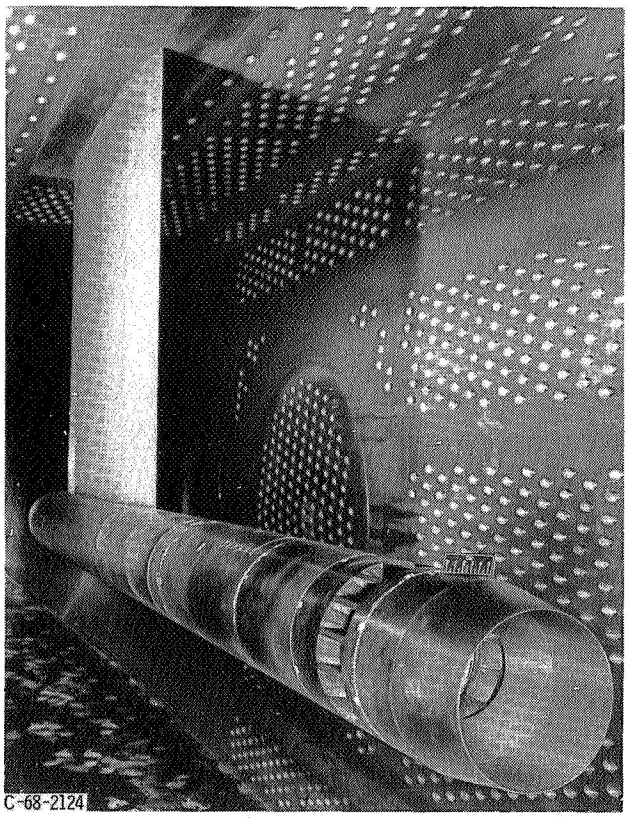

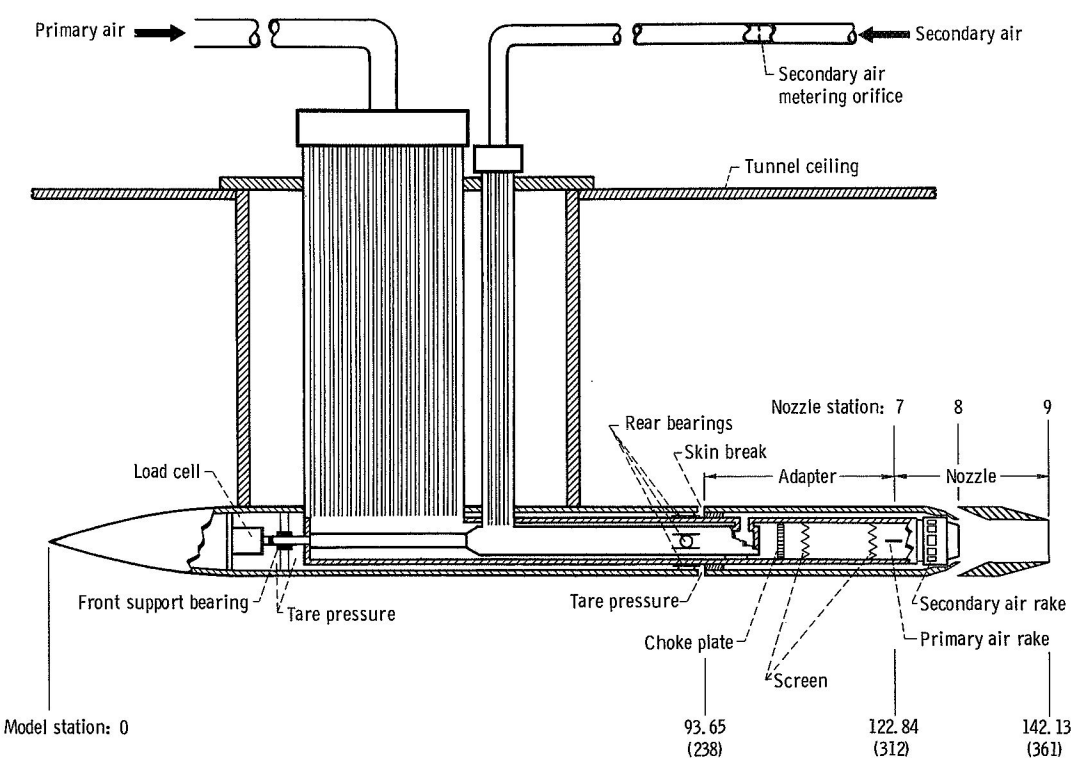

Figure 1. - Nozzle support model and thrust measuring system. (Dimensions are in inches (cm).)

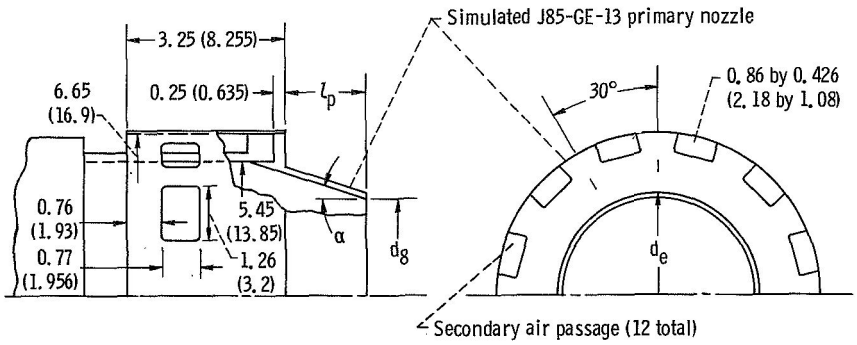

Primary nozzle configuration	Primary nozzle length, l_p		Primary nozzle diameter, d_8		Primary nozzle flap angle, α, deg	Flow coefficient, C_{D8}	External diameter of primary nozzle lip, d_e	
	in.	cm	in.	cm			in.	cm
I - Subsonic cruise and dry acceleration	1.50	3.810	4.388	11.146	13.25	0.977	4.622	11.74
II - Maximum reheat acceleration	1.08	2.743	5.192	13.188	5.30	0.985	5.437	13.81

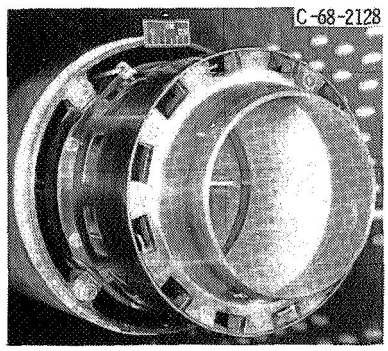

Figure 2. - Details of simulated J85-GE-13 primary nozzle. Dimensions are in inches (cm).)

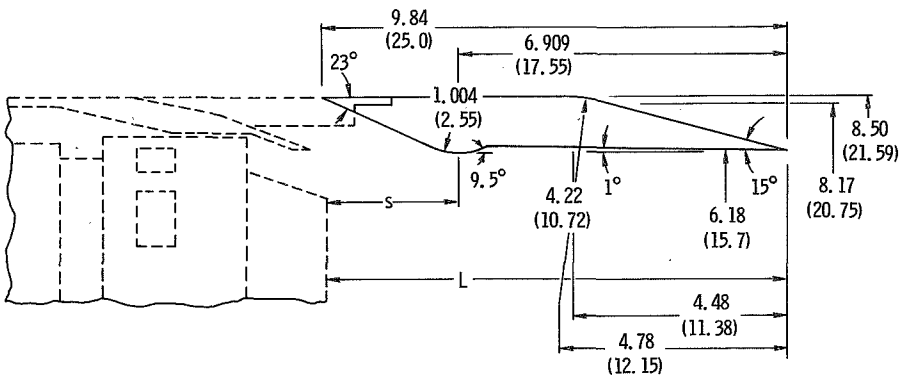

Primary nozzle configuration	Internal area ratio, A_9/A_8	Spacing ratio, s/d_8	Throat diameter ratio, d_s/d_8	Flap length ratio, L/d_8	L		s	
					in.	cm	in.	cm
I - Subsonic cruise and dry acceleration	1.99	0.585	1.408	2.16	9.477	24.07	2.566	6.52
II - Reheat acceleration	1.42	0.575	1.190	1.91	9.897	25.14	2.986	7.58

Figure 3. - Details of triple-hinge trailing flap. Ratio of boattail area to simulated nacelle area, A_β/A_{max} = 0.47. (Dimensions are in inches (cm).)

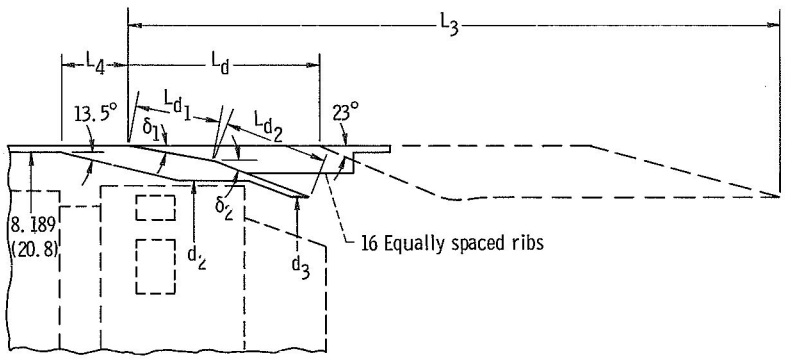

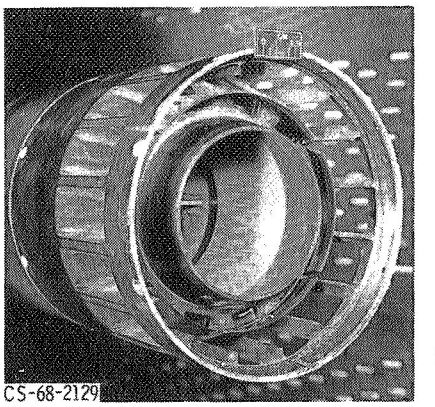

Door configuration	δ_1	δ_2	L_d		d_2		d_3		l_3		Aspect ratio, AR_d	Ratio of tertiary flow area to shroud exit area, A_{ter}/A_9	L_4		L_{d_1}		L_{d_2}	
			in.	cm	in.	cm	in.	cm	in.	cm			in.	cm	in.	cm	in.	cm
Double, full open	10°	20°	3.972	10.09	7.0	17.78	6.386	16.22	13.78	35.00	0.306	0.715	1.369	3.48	1.895	4.81	2.040	5.13
	8°	16°	3.961	10.06	7.0	17.78	6.81	17.30	13.744	34.91	.305	.584	1.405	3.57	1.860	4.72	2.040	5.13
	5°	10°	3.854	9.79	7.441	18.90	7.441	18.90	13.634	34.63	.297	.368	1.513	3.84	1.753	4.45	2.040	5.13
Single, full open	20°	---	3.035	7.71	7.0	17.78	6.386	16.22	12.819	32.56	0.234	0.715	2.330	5.92	3.003	7.63	-----	----
	16°	---	3.024	7.68	7.0	17.78	6.81	17.30	12.803	32.52	.233	.584	2.345	5.96	2.978	7.56	-----	----
	10°	---	2.972	7.55	7.441	18.9	7.441	18.9	12.752	32.39	.229	.368	2.392	6.08	2.919	7.41	-----	----
Closed	---	---	2.968	7.54	8.189	20.8	8.189	20.8	-----	-----	----	-----	-----	----	-----	----	-----	----

(a) Details of auxiliary inlets. (Dimensions are in inches (cm).)

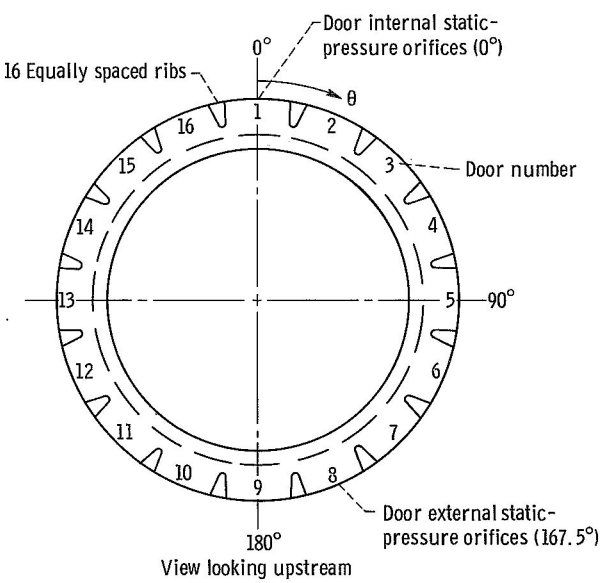

(b) End view of auxiliary inlets.

Figure 4. - Auxiliary inlets.

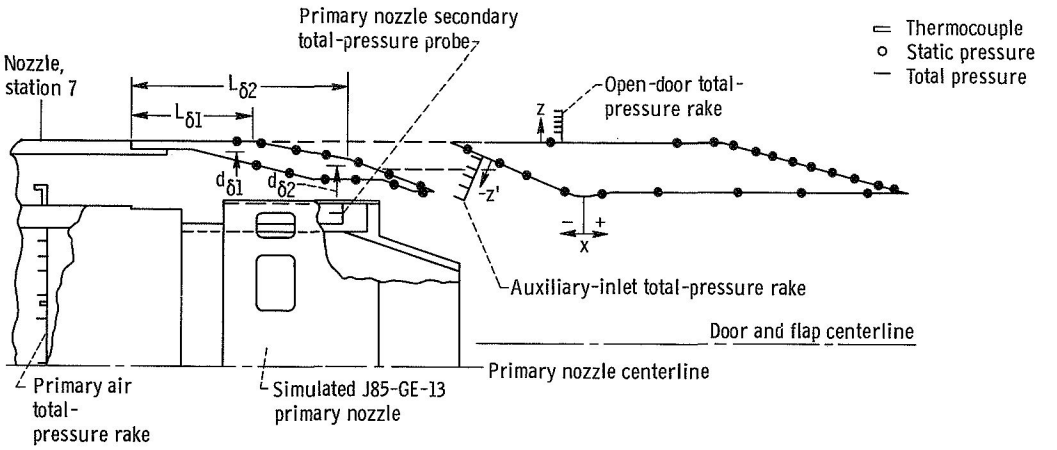

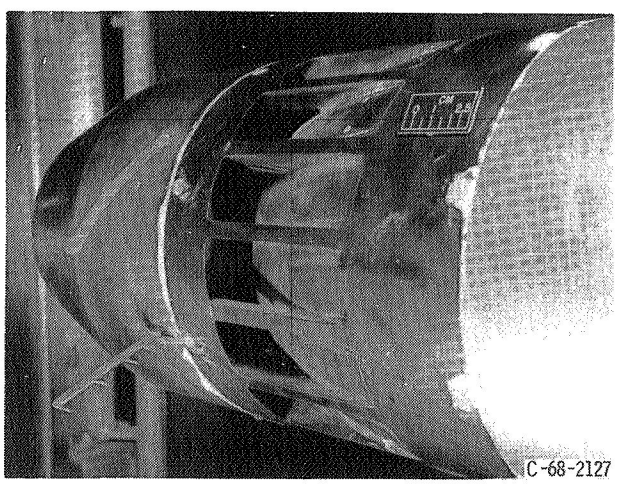

(a) Instrumentation layout.

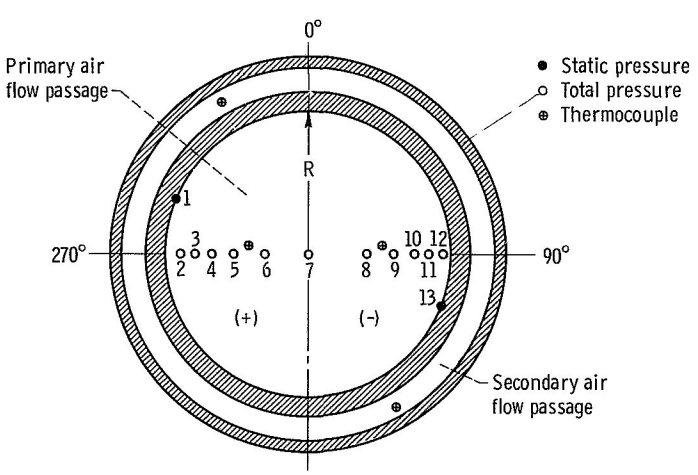

Primary flow orifice number	Normalized distance from centerline, r/R
1	1.00
2	.90
3	.790
4	.670
5	.519
6	.30
7	0
8	-.418
9	-.600
10	-.750
11	-.855
12	-.950
13	-1.00

(b) Details of instrumentation at station 7 (view looking downstream). Radius, R = 3.006 inches (7.635 cm); r is radius from center to local probe.

Figure 5. - Auxiliary inlet ejector nozzle instrumentation. See figure 5(b) for details of instrumentation at station 7. See table III for locations of total-pressure probes. See table II for door static-pressure orifice locations. See table IV for trailing-flap static-pressure orifice locations. See table I for door hinge location.

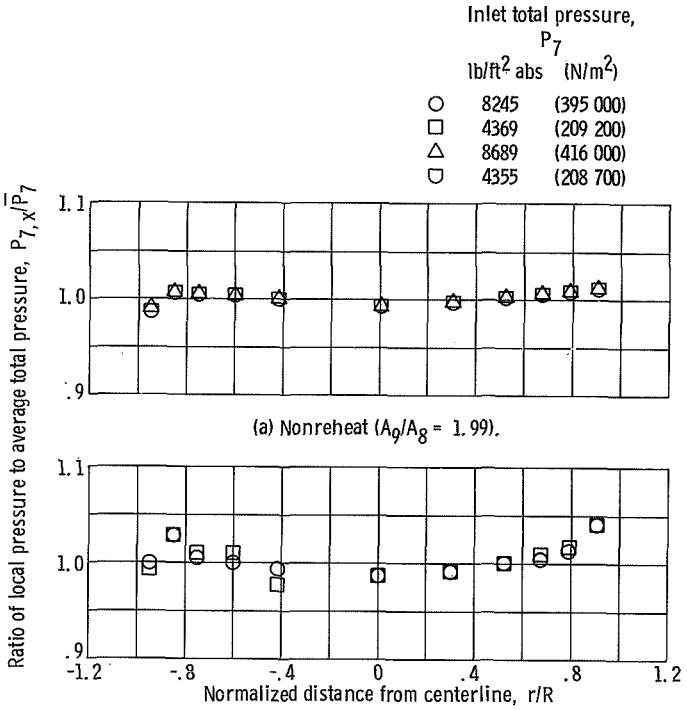

(a) Nonreheat (A_9/A_8 = 1.99).

(b) Maximum reheat (A_9/A_8 = 1.42).

Figure 6. - Primary total-pressure profile at station 7.

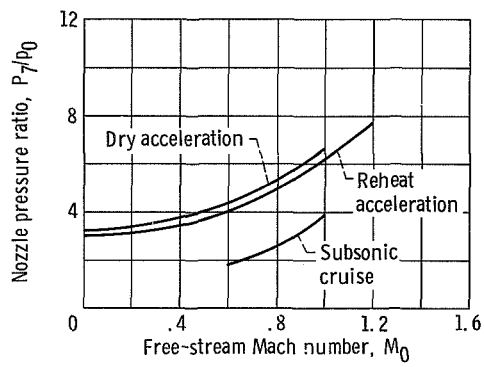

Figure 7. - Schedule of turbojet nozzle pressure ratio with free-stream Mach number.

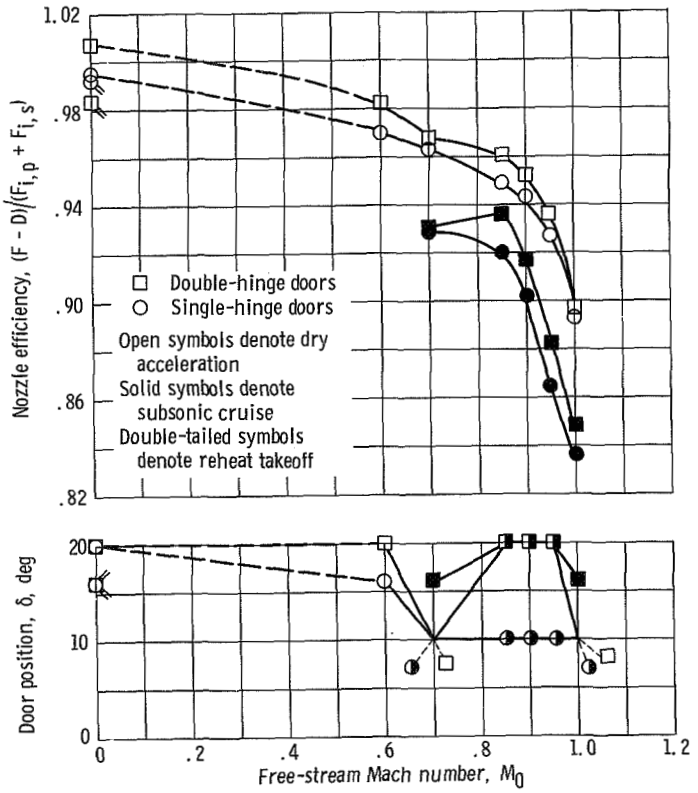

Figure 8. - Comparison of best measured nozzle efficiencies of single- and double-hinge door configurations. Corrected secondary-weight-flow-rate ratio, $\omega\sqrt{\tau} = 0.04$. (Double-hinge door position is denoted by downstream door position δ_2.)

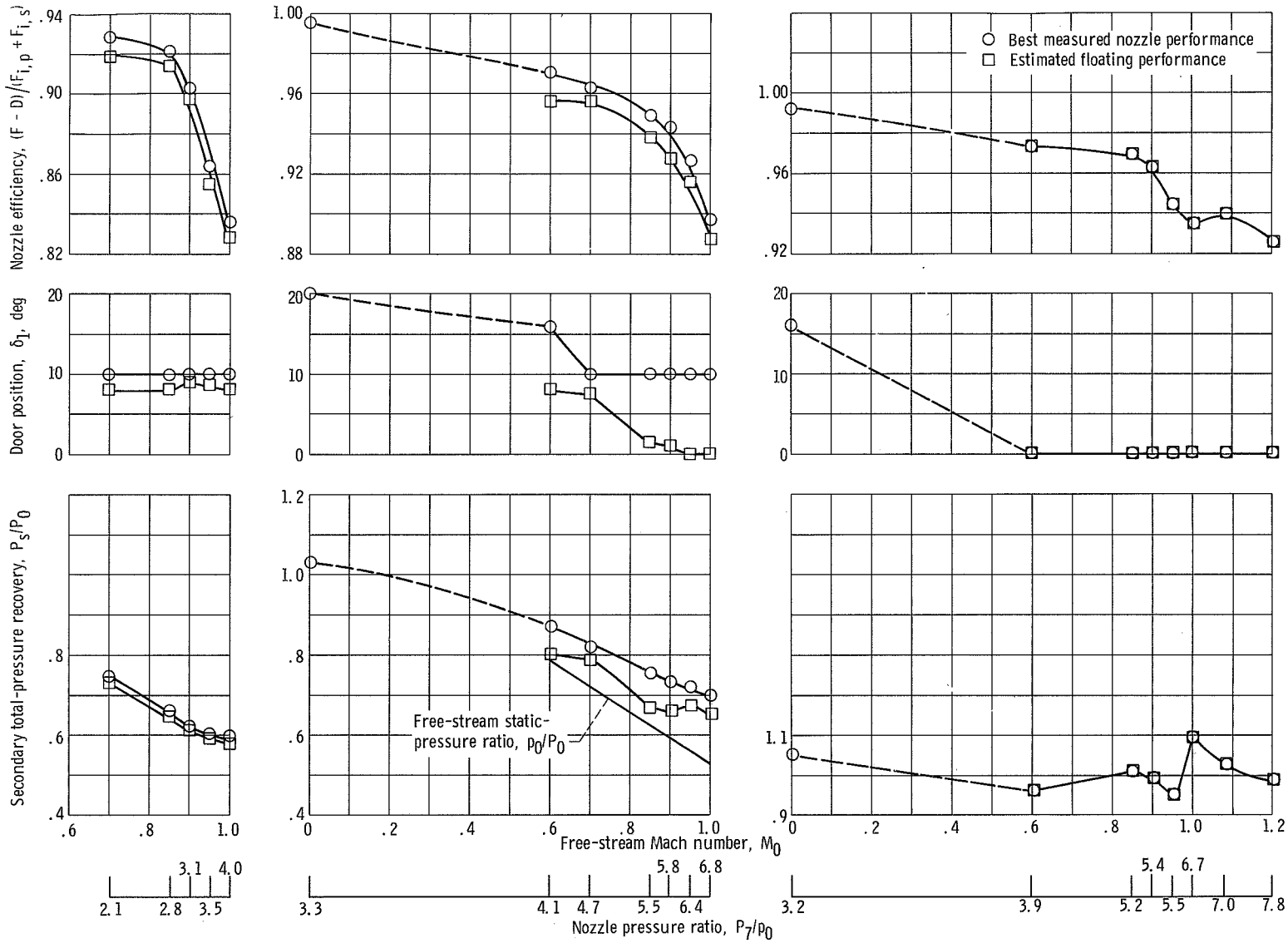

(a) Subsonic cruise (A_9/A_8 = 1.99).

(b) Dry acceleration (A_9/A_8 = 1.99).

(c) Maximum reheat acceleration (A_9/A_8 = 1.42).

Figure 9. - Performance and total-pressure recovery requirements of single-hinge door configurations. Corrected secondary-weight-flow-rate ratio, $\omega\sqrt{\tau}$ = 0.04.

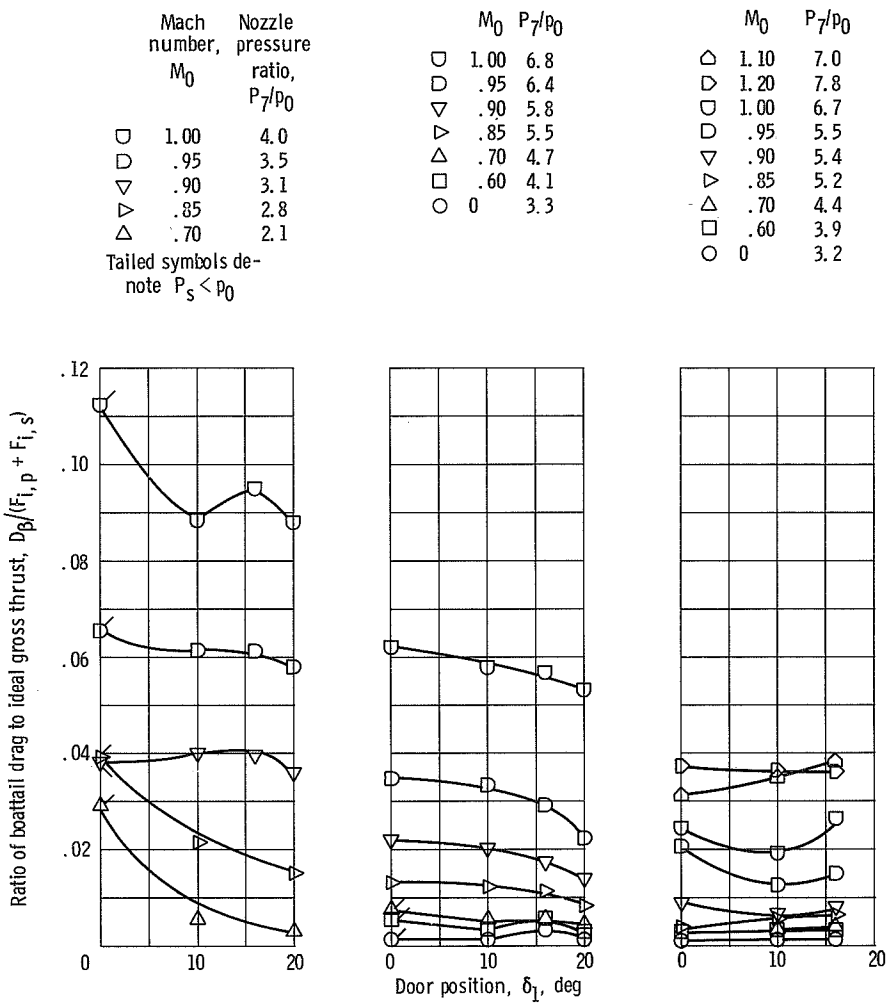

(a) Subsonic cruise (A_9/A_8 = 1.99).

(b) Dry acceleration (A_9/A_8 = 1.99).

(c) Maximum reheat acceleration (A_9/A_8 = 1.42).

Figure 10. - Effect of single-hinge door position on boattail-drag-to-ideal-gross-thrust ratio.

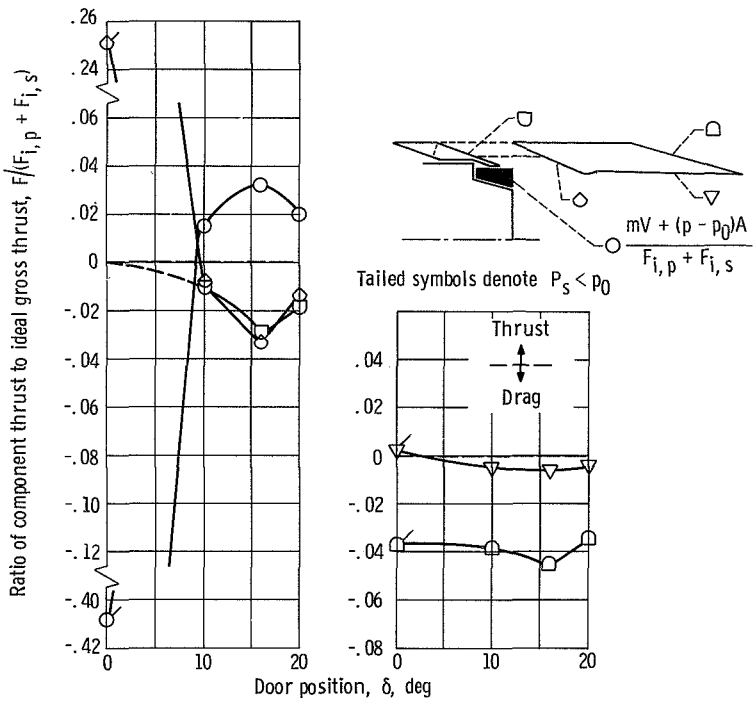

Figure 11. - Effect of single-hinge door position on component-thrust-to-ideal gross thrust ratio. Subsonic cruise; corrected secondary-weight-flow-rate ratio, $\omega\sqrt{\tau} = 0.04$; nozzle pressure ratio, $P_7/p_0 = 3.10$; free-stream Mach number, $M_0 = 0.90$.

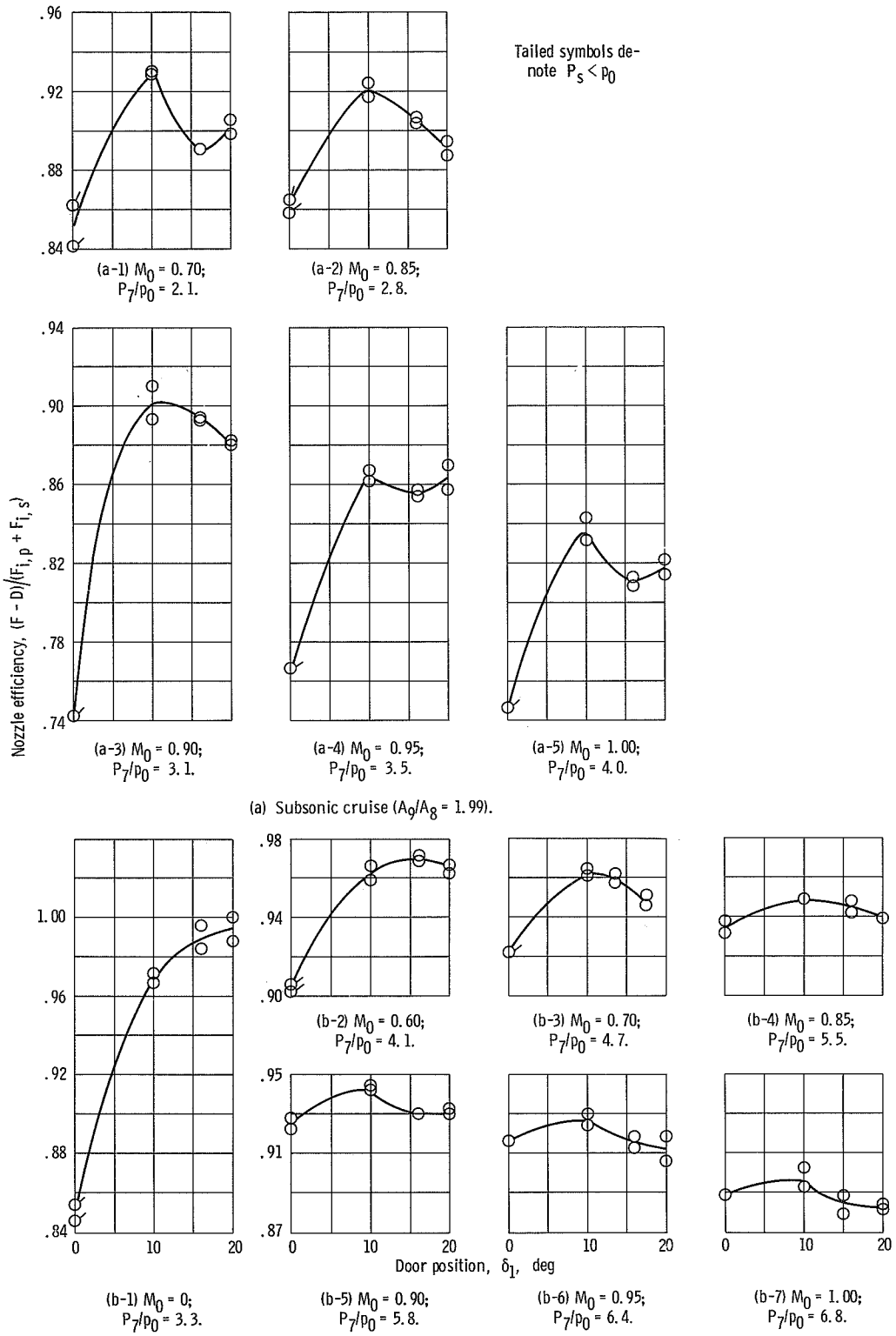

Figure 12. - Effect of single-hinge door position on nozzle efficiency. Corrected secondary-weight-flow-rate ratio, $\omega\sqrt{\tau} = 0.04$.

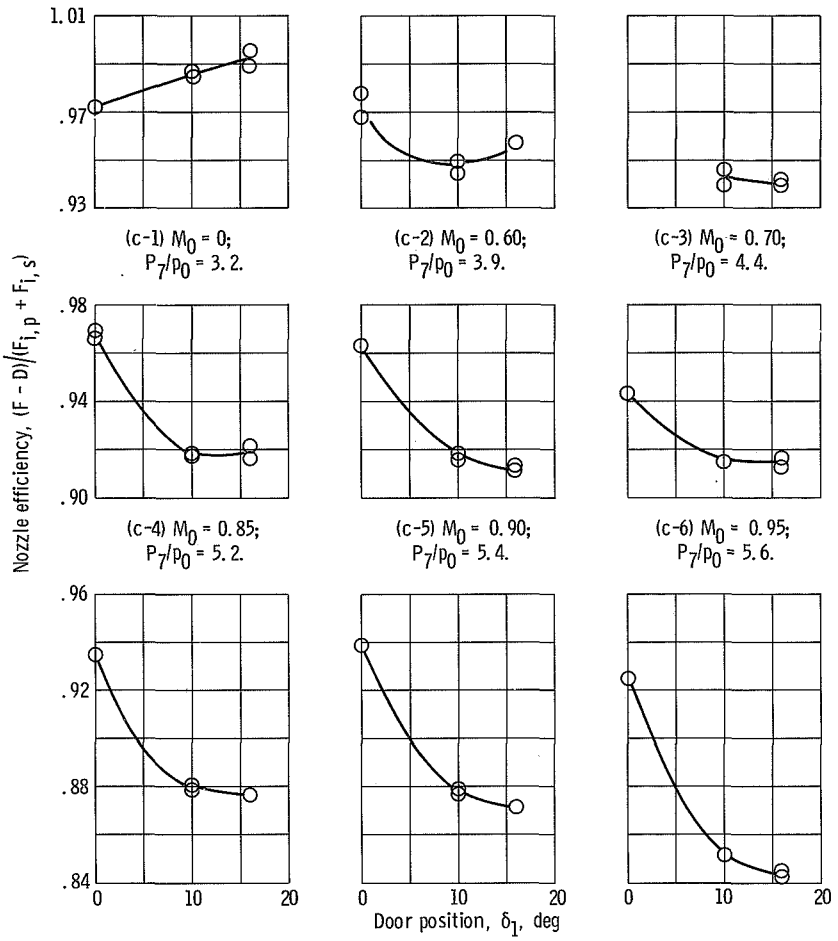

(c) Maximum reheat acceleration (A_9/A_8 = 1.42).

Figure 12. - Concluded.

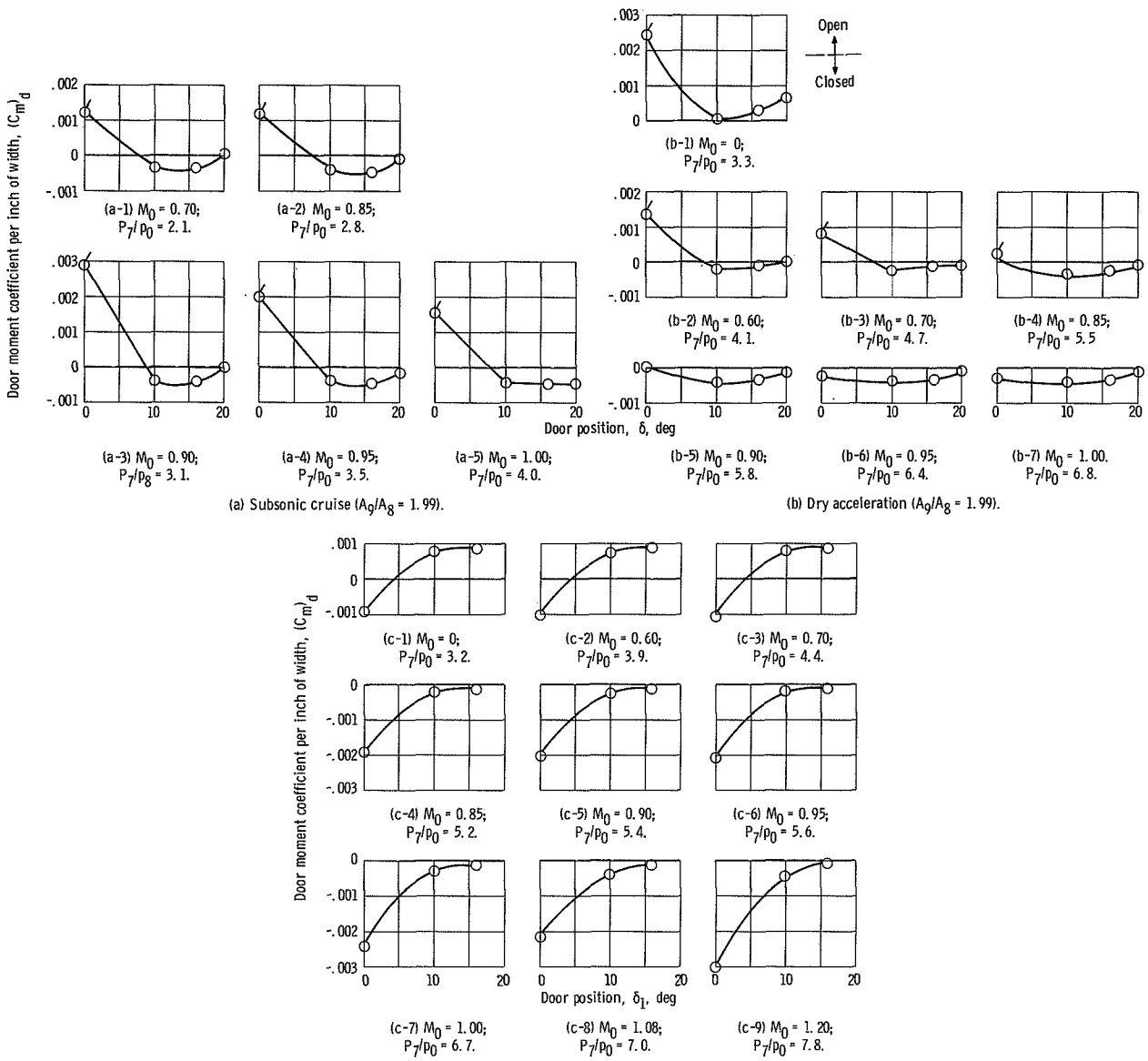

Figure 13. - Effect of single-hinge door position on door moment coefficient, $(C_m)_d = (M_{ext} - M_{int})/(A_{max})(d_{max})(P_7)$. Corrected secondary-weight-flow-rate ratio, $\omega\sqrt{\tau} = 0.04$.

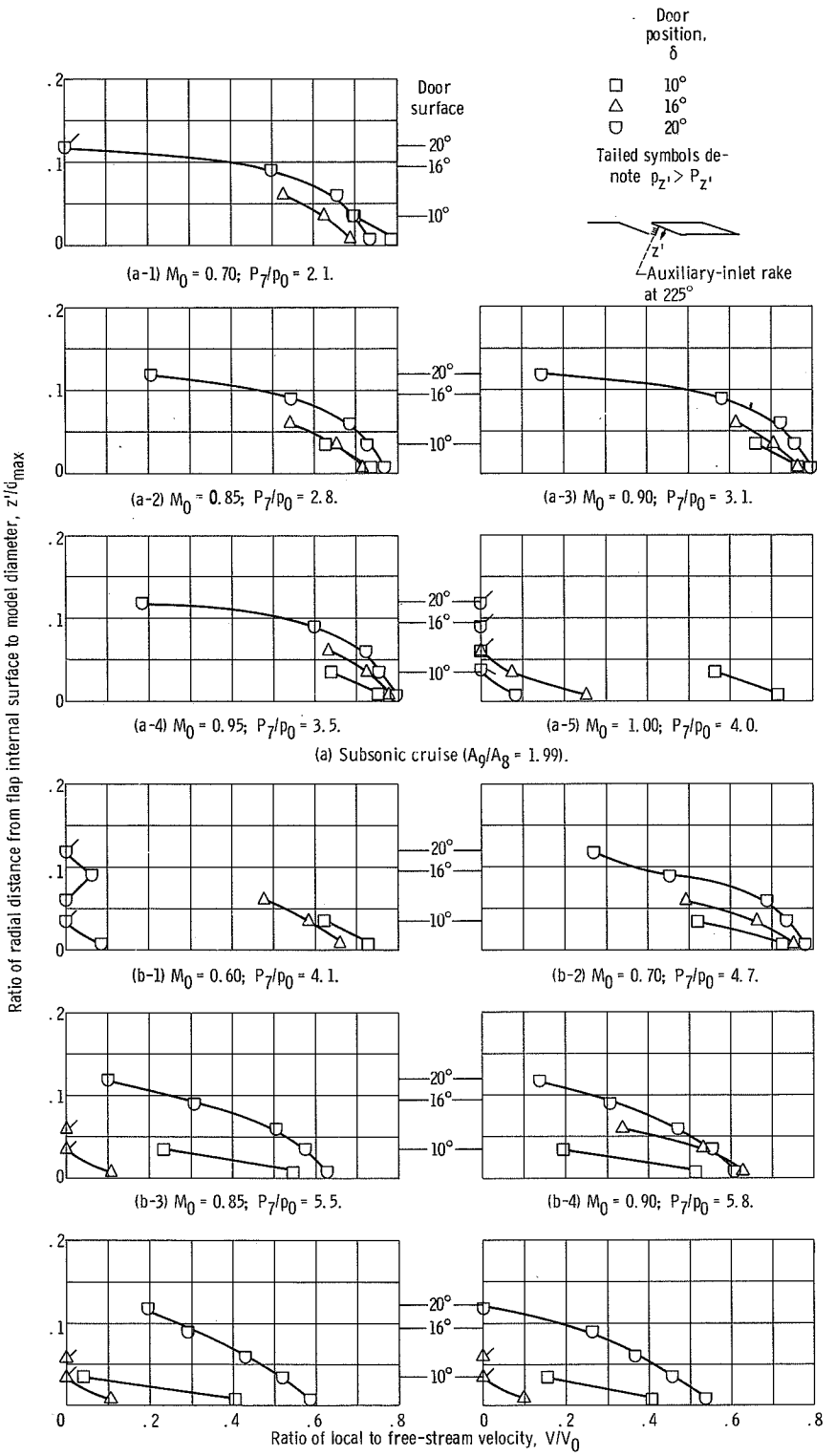

Figure 14. - Effect of single-hinge door position on auxiliary inlet flow velocity. Corrected secondary-weight-flow-rate ratio, $\omega\sqrt{\tau}$ = 0.04.

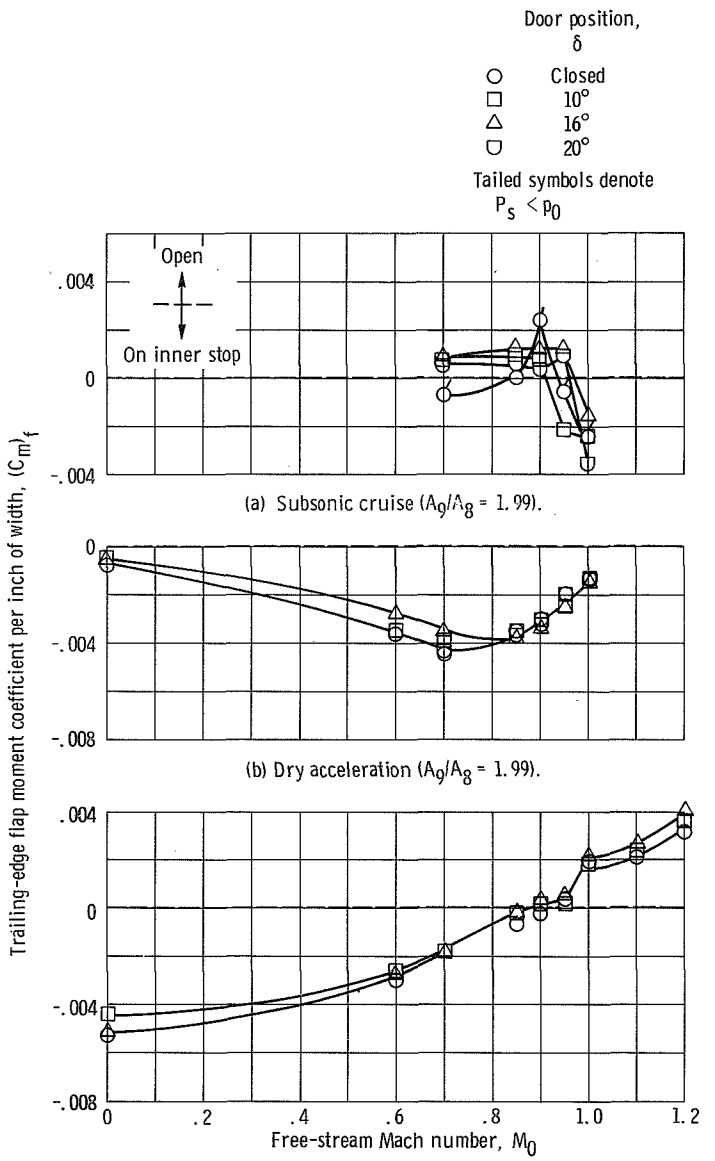

(a) Subsonic cruise (A_9/A_8 = 1.99).

(b) Dry acceleration (A_9/A_8 = 1.99).

(c) Maximum reheat acceleration (A_9/A_8 = 1.42).

Figure 15. - Effect of single-hinge door position on trailing-edge flap moment coefficient per inch of width, $(C_m)_f = M_{TR}/(A_{max})(d_{max})(P_7)$.

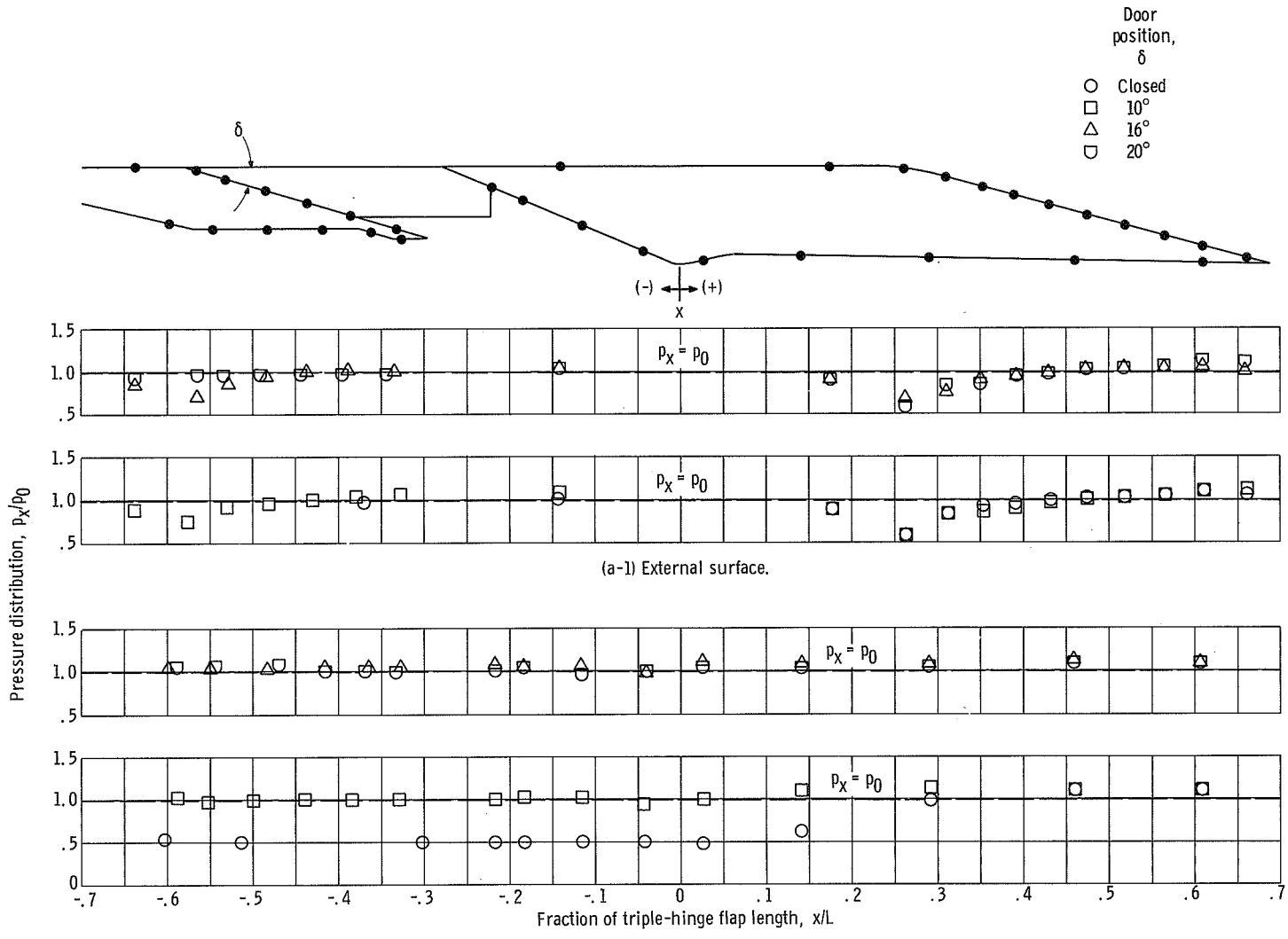

(a-1) External surface.

(a-2) Internal surface.

(a) Subsonic cruise ($A_9/A_8 = 1.99$); nozzle pressure ratio, $P_7/p_0 = 3.1$; free-stream Mach number, $M_0 = 0.90$.

Figure 16. - Effect of single-hinge door position on auxiliary inlet nozzle pressure distribution. Corrected secondary-weight-flow-rate ratio, $\omega\sqrt{\tau} = 0.04$.

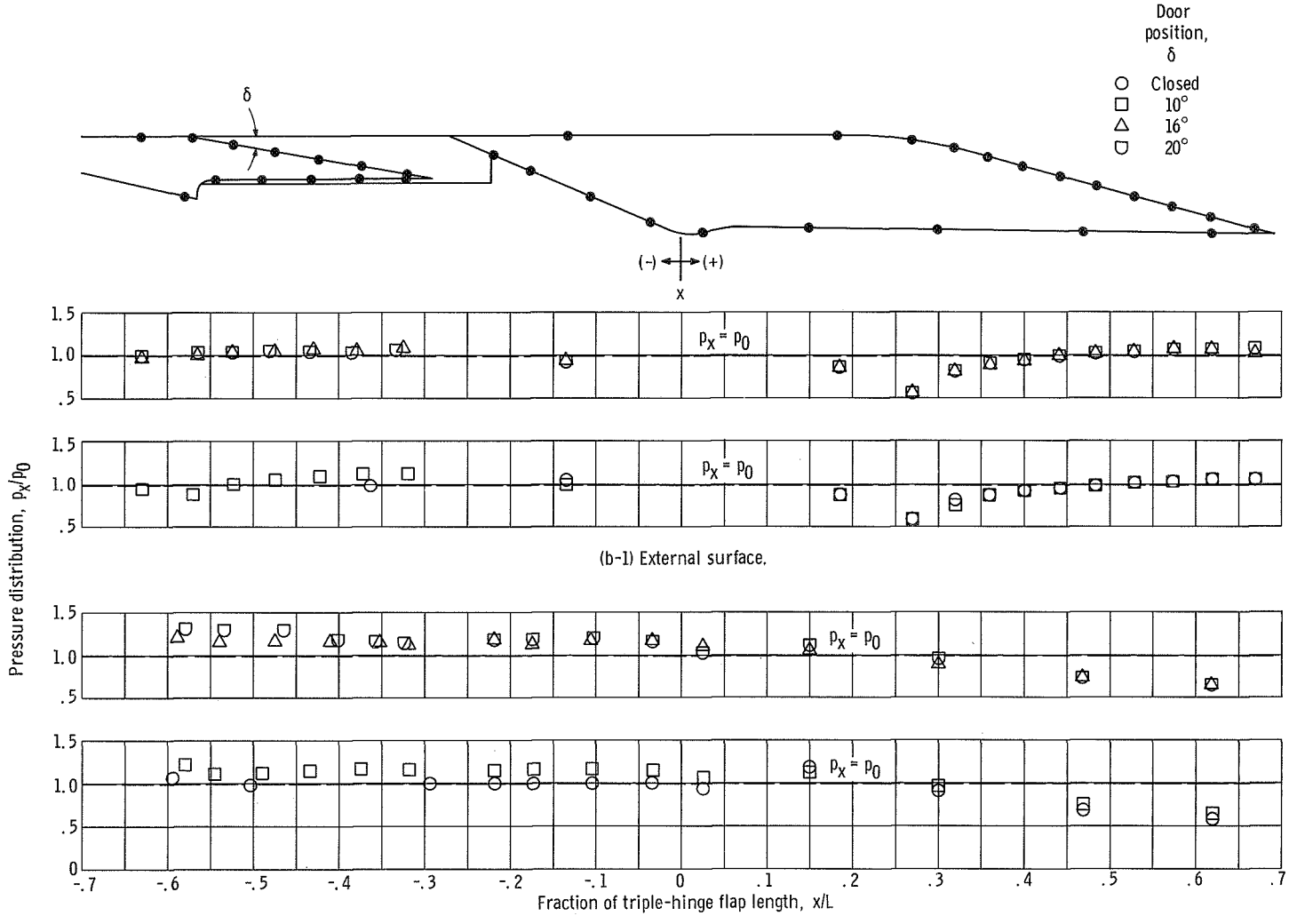

(b-1) External surface.

(b-2) Internal surface.

(b) Dry acceleration (A_9/A_8 = 1.99); nozzle pressure ratio, P_7/p_0 = 5.8; free-stream Mach number, M_0 = 0.90.

Figure 16. - Continued.

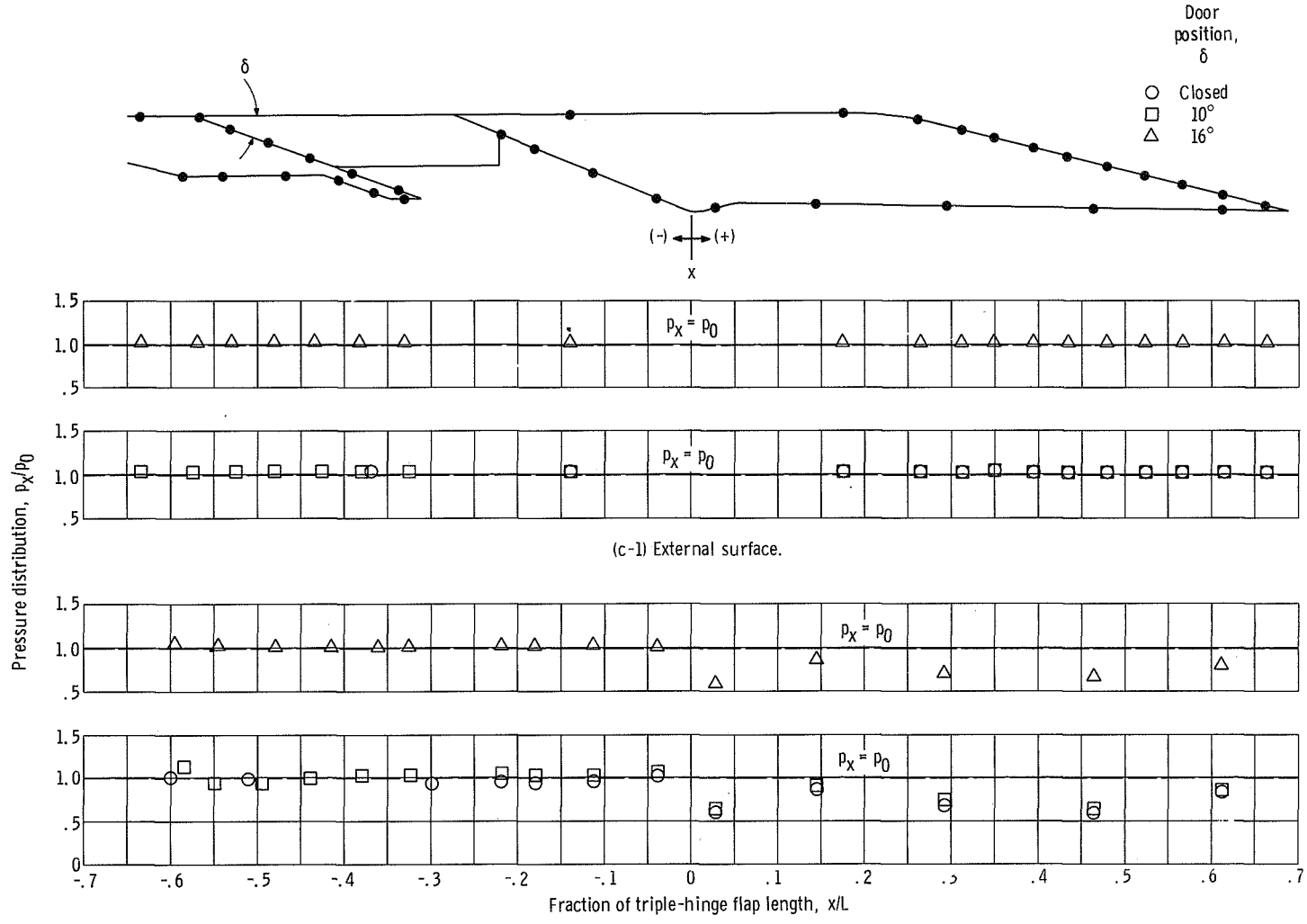

(c-1) External surface.

(c-2) Internal surface.

(c) *Maximum reheat acceleration* ($A_9/A_8 = 1.42$); *nozzle pressure ratio,* $P_7/p_0 = 3.2$; *free-stream Mach number,* $M_0 = 0$.

Figure 16. - Continued.

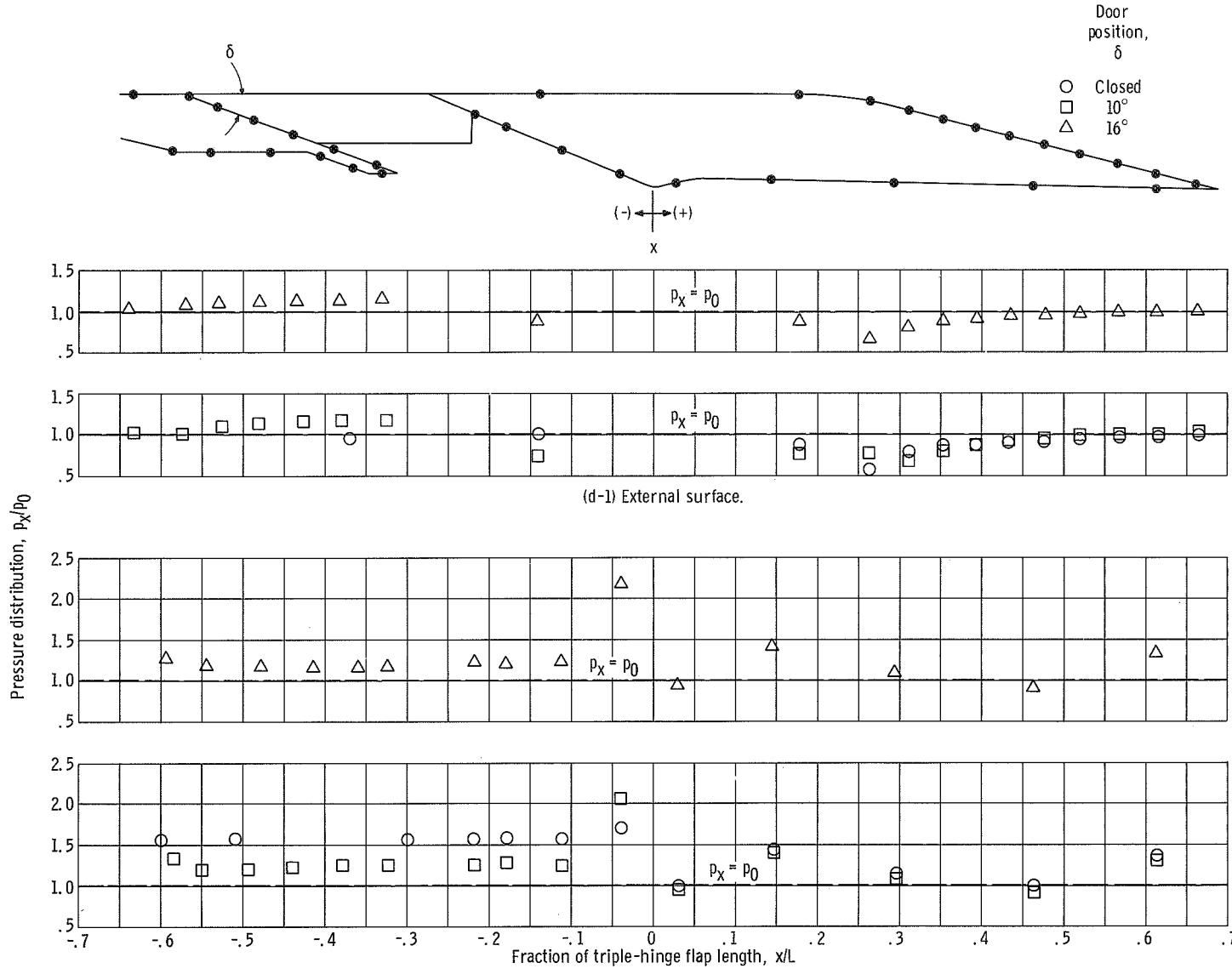

(d-1) External surface.

(d-2) Internal surface.

(d) Maximum reheat acceleration (A_9/A_8 = 1.42); nozzle pressure ratio, P_7/p_0 = 5.6; free-stream Mach number, M_0 = 0.95.

Figure 16. - Concluded.

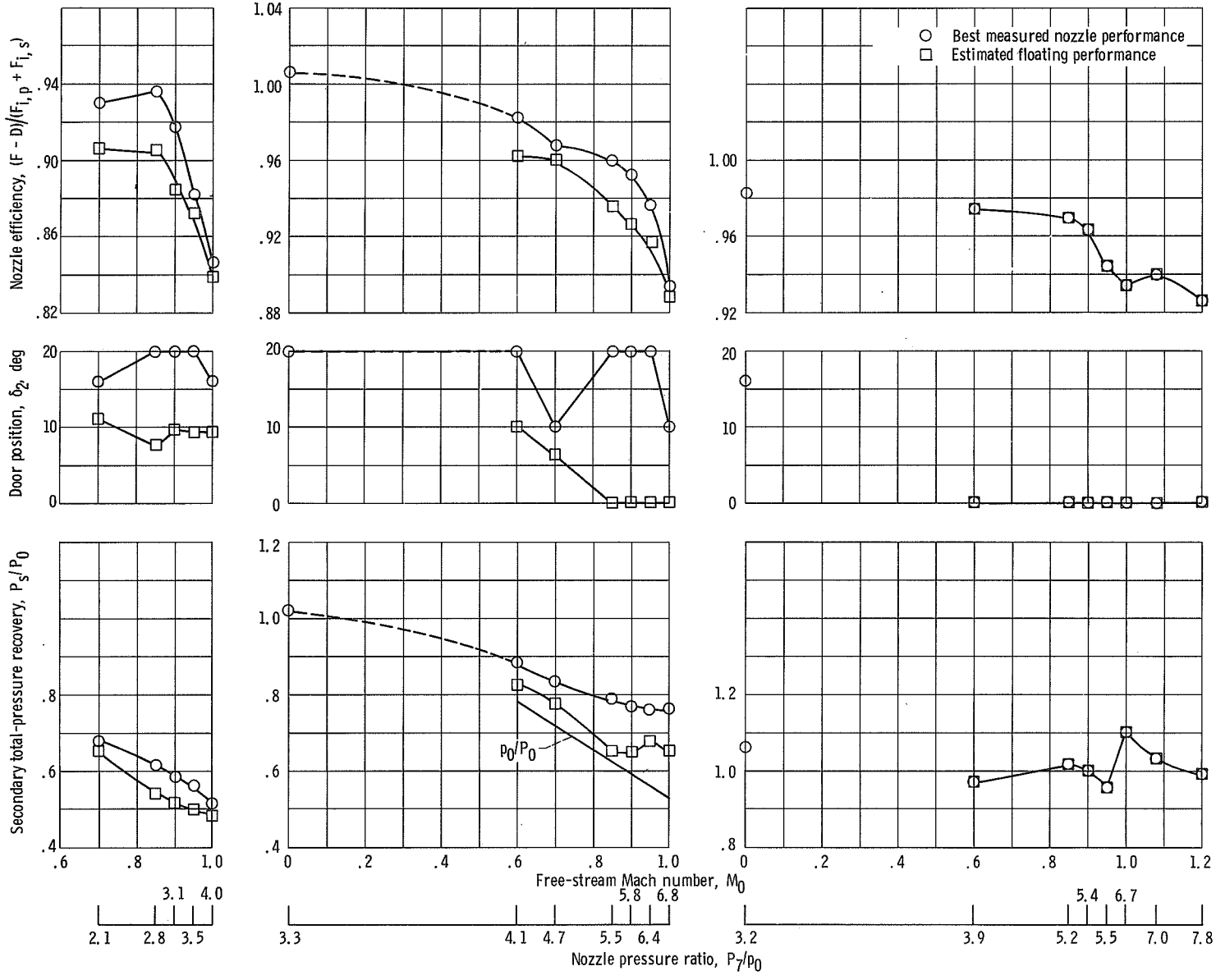

(a) Subsonic cruise ($A_9/A_8 = 1.99$).

(b) Dry acceleration ($A_9/A_8 = 1.99$).

(c) Maximum reheat acceleration ($A_9/A_8 = 1.42$).

Figure 17. - Performance and total-pressure recovery requirements of double-hinge door configurations. Corrected secondary-weight-flow-rate ratio, $\omega\sqrt{\tau} = 0.04$.

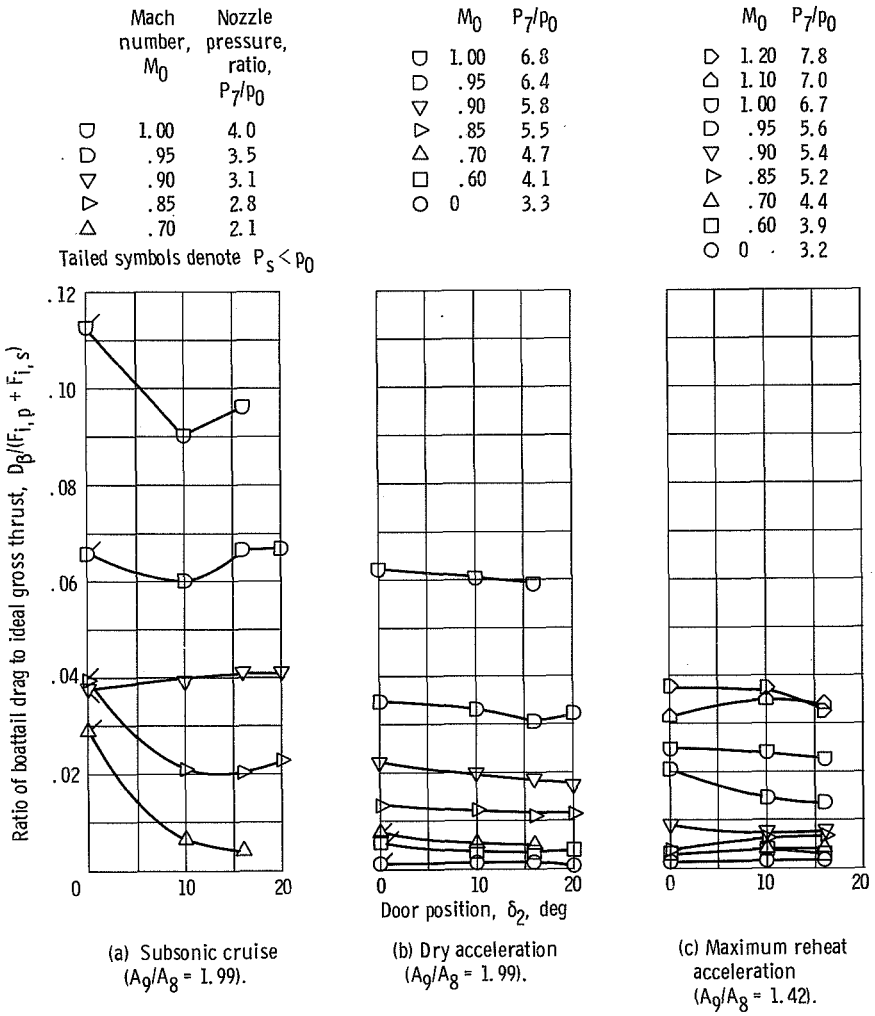

(a) Subsonic cruise ($A_9/A_8 = 1.99$).

(b) Dry acceleration ($A_9/A_8 = 1.99$).

(c) Maximum reheat acceleration ($A_9/A_8 = 1.42$).

Figure 18. - Effect of double-hinge door position on boattail-drag-to-ideal-gross-thrust ratio.

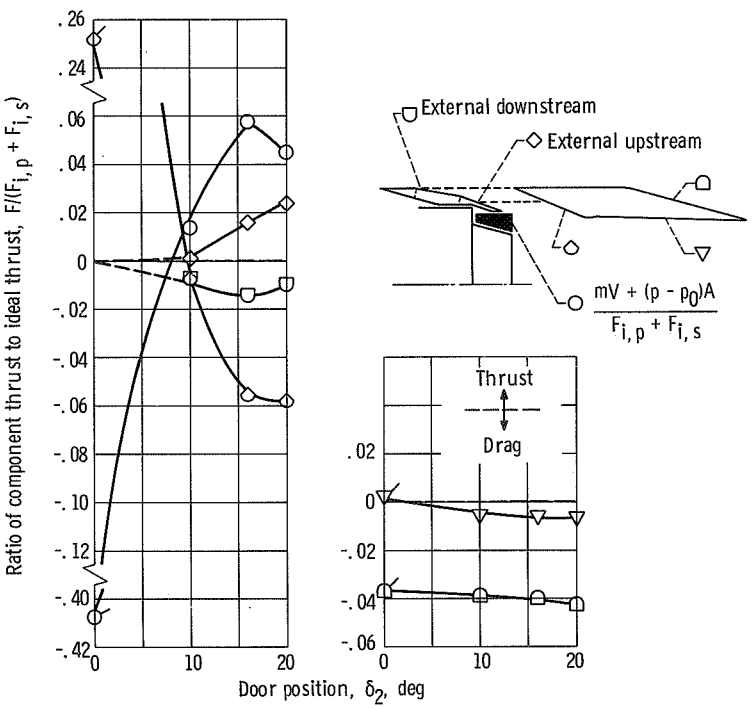

Figure 19. - Effect of double-hinge door position on component-thrust-to-ideal-gross-thrust ratio. Subsonic cruise; corrected secondary-weight-flow-rate ratio, $\omega\sqrt{\tau} = 0.04$; nozzle pressure ratio, $P_7/p_0 = 3.10$; free-stream Mach number, $M_0 = 0.90$.

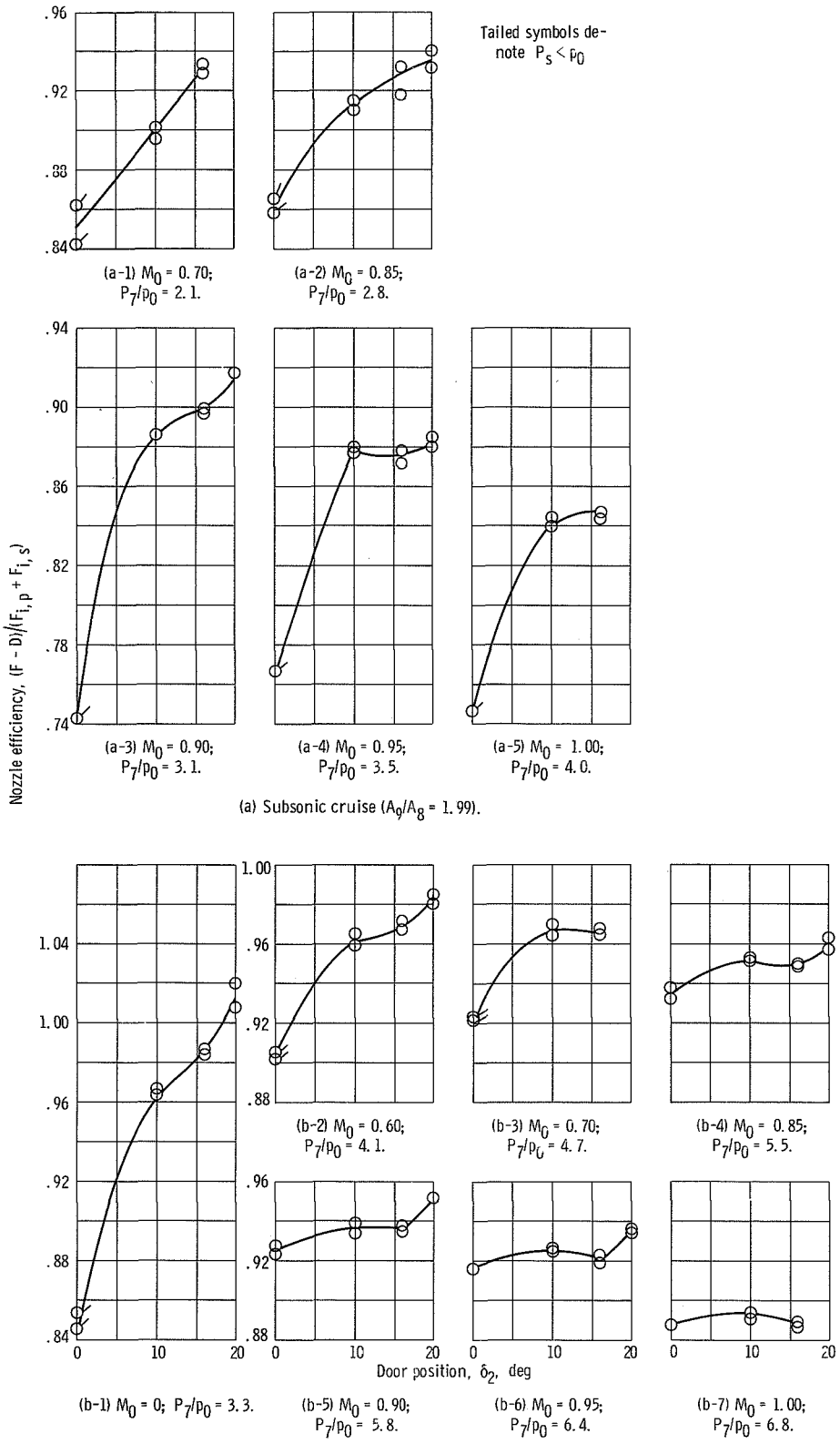

Figure 20. - Effect of double-hinge door position on nozzle efficiency. Corrected secondary-weight-flow-rate ratio, $\omega\sqrt{\tau} = 0.040$.

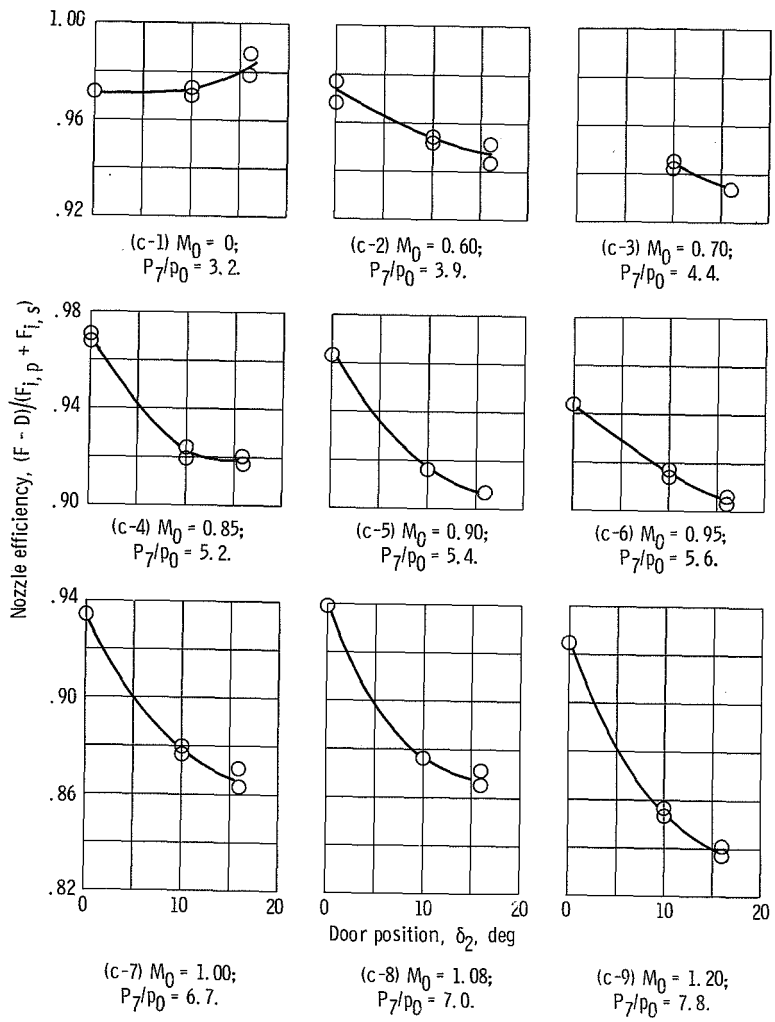

(c) Maximum reheat acceleration (A_9/A_8 = 1.42).

Figure 20. - Concluded.

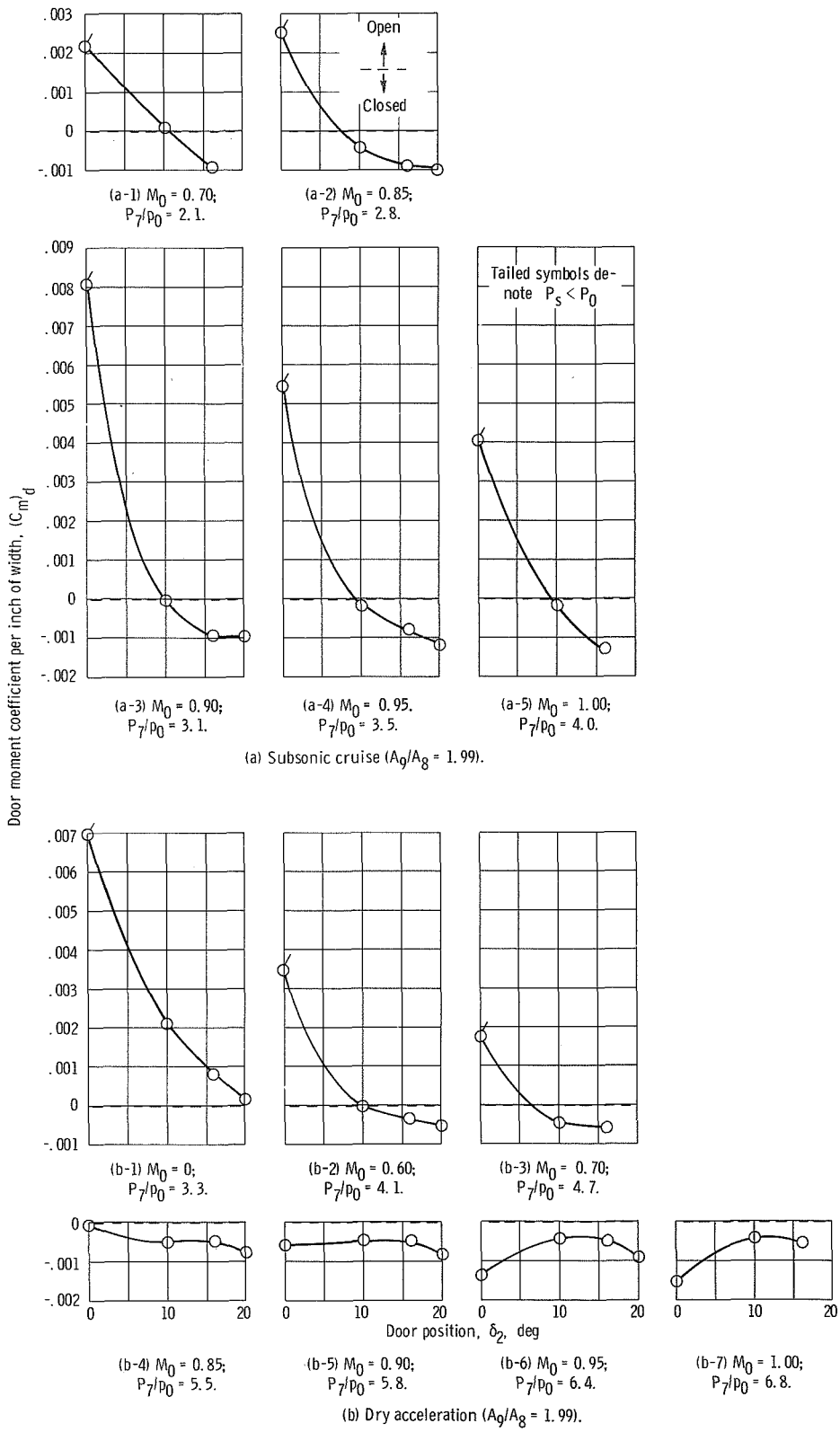

Figure 21. - Effect of double-hinge door position on door moment coefficient, $(C_m)_d = (M_{ext} - M_{int})/(A_{max})(d_{max})(P_7)$. Corrected secondary-weight-flow-rate ratio, $\omega\sqrt{\tau} = 0.04$.

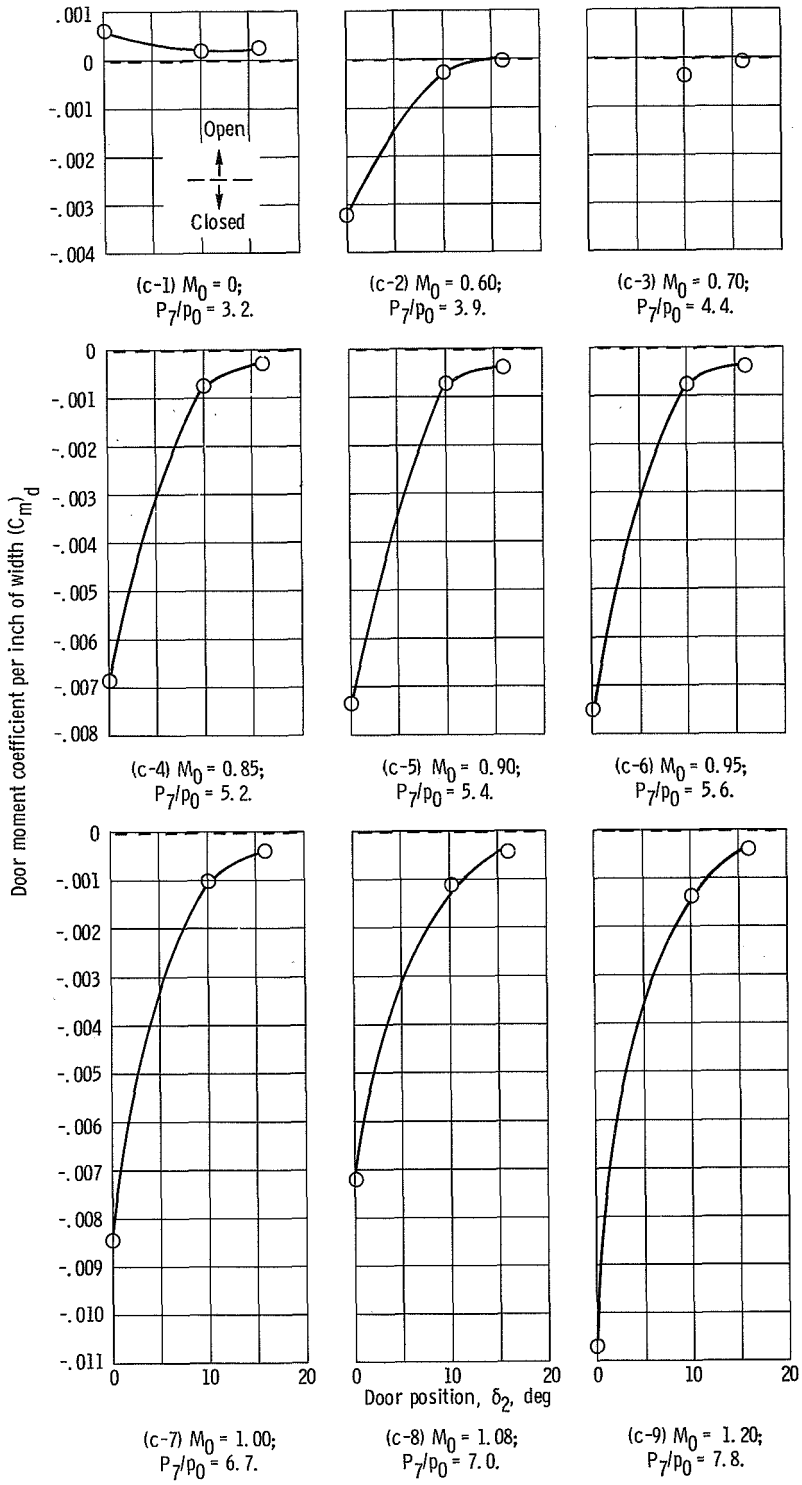

(c) Maximum reheat acceleration (A_9/A_8 = 1.42).

Figure 21. - Concluded.

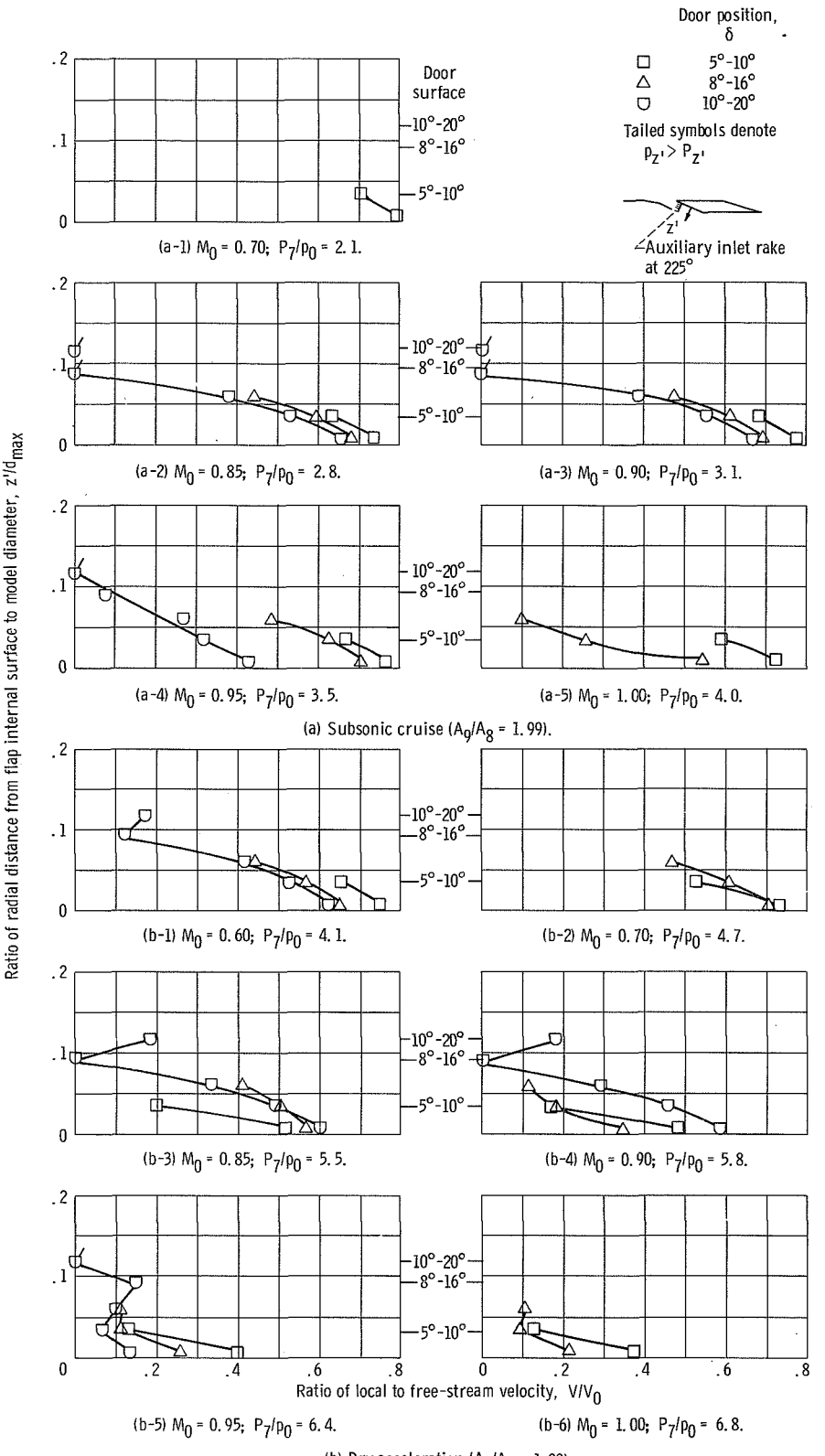

Figure 22. - Effect of double-hinge door position on auxiliary-inlet flow velocity. Corrected secondary-weight-flow-rate ratio, $\omega\sqrt{\tau} = 0.04$.

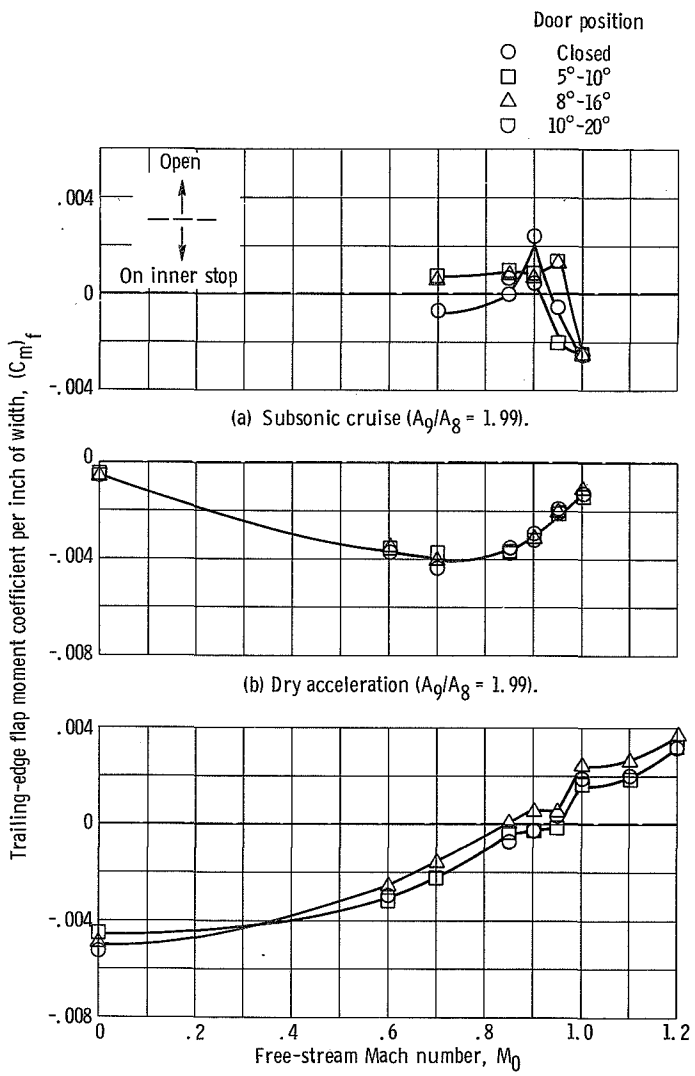

(a) Subsonic cruise (A_9/A_8 = 1.99).

(b) Dry acceleration (A_9/A_8 = 1.99).

(c) Maximum reheat acceleration (A_9/A_8 = 1.42).

Figure 23. - Effect of double-hinge door position on trailing-edge flap moment coefficient per inch of width, $(C_m)_f = M_{TR}/(A_{max})(d_{max})(P_7)$.

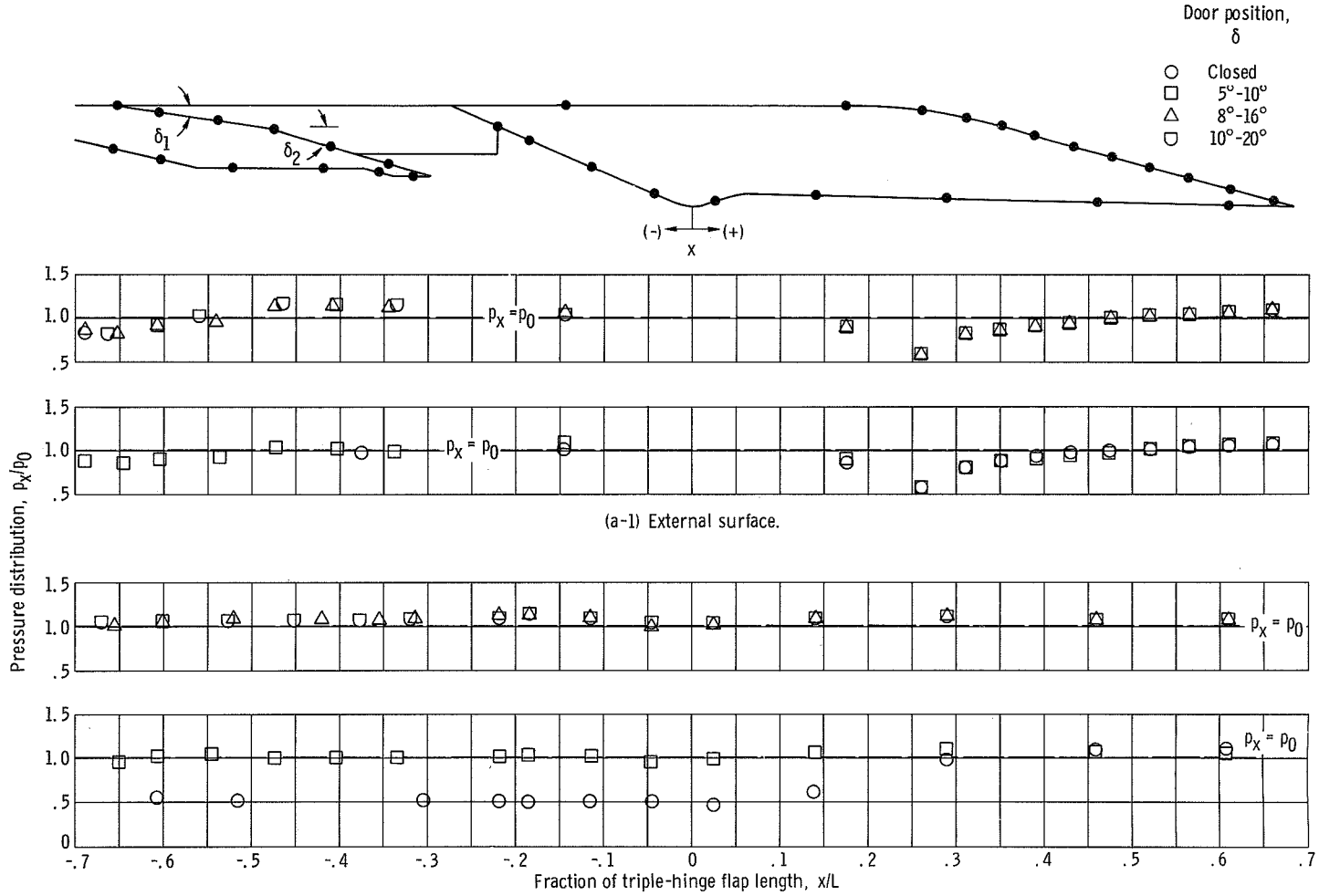

(a-1) External surface.

(a-2) Internal surface.

(a) Subsonic cruise (A_9/A_8 = 1.99); nozzle pressure ratio, P_7/p_0 = 3.1; free-stream Mach number, M_0 = 0.90.

Figure 24. - Effect of double-hinge door position on auxiliary inlet nozzle pressure distribution. Corrected secondary-weight-flow-rate ratio, $\omega\sqrt{\tau}$ = 0.04.

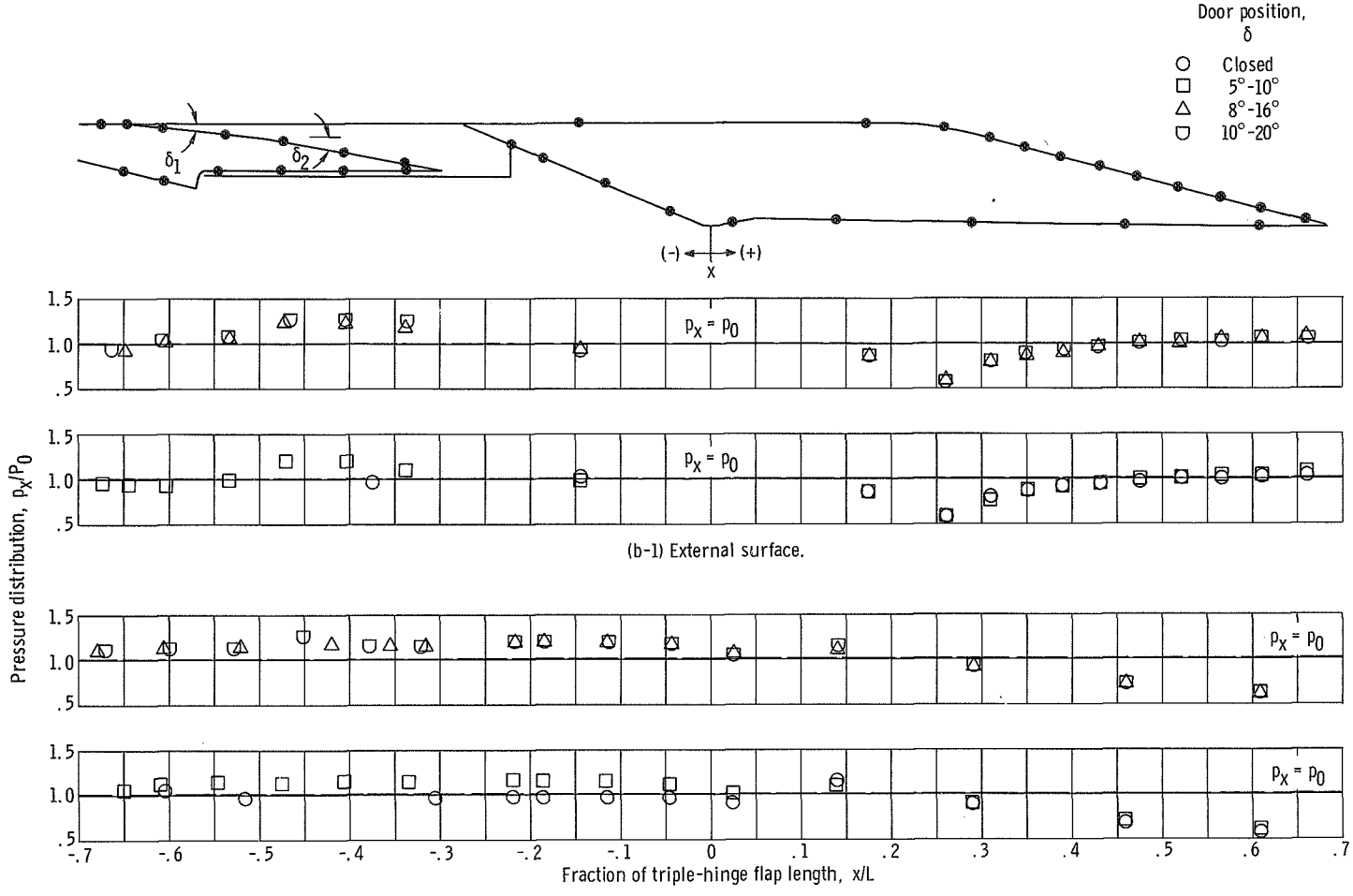

(b-1) External surface.

(b-2) Internal surface.

(b) Dry acceleration ($A_9/A_8 = 1.99$); nozzle pressure ratio $P_7/p_0 = 5.8$; free-stream Mach number, $M_0 = 0.90$.

Figure 24. - Continued.

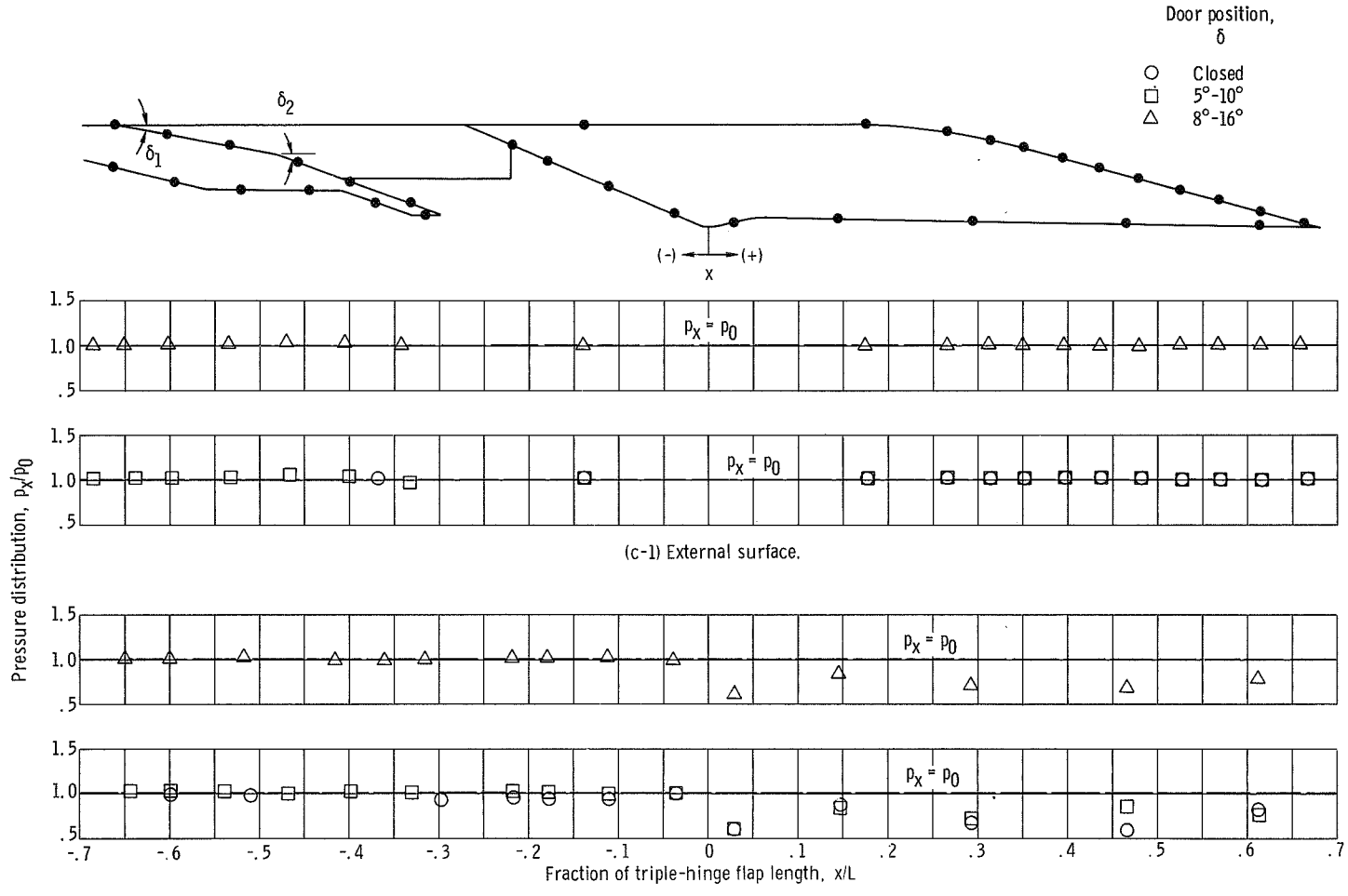

(c-1) External surface.

(c-2) Internal surface.

(c) Maximum reheat acceleration ($A_9/A_8 = 1.42$); nozzle pressure ratio, $P_7/p_0 = 3.20$; free-stream Mach number, $M_0 = 0$.

Figure 24. - Continued.

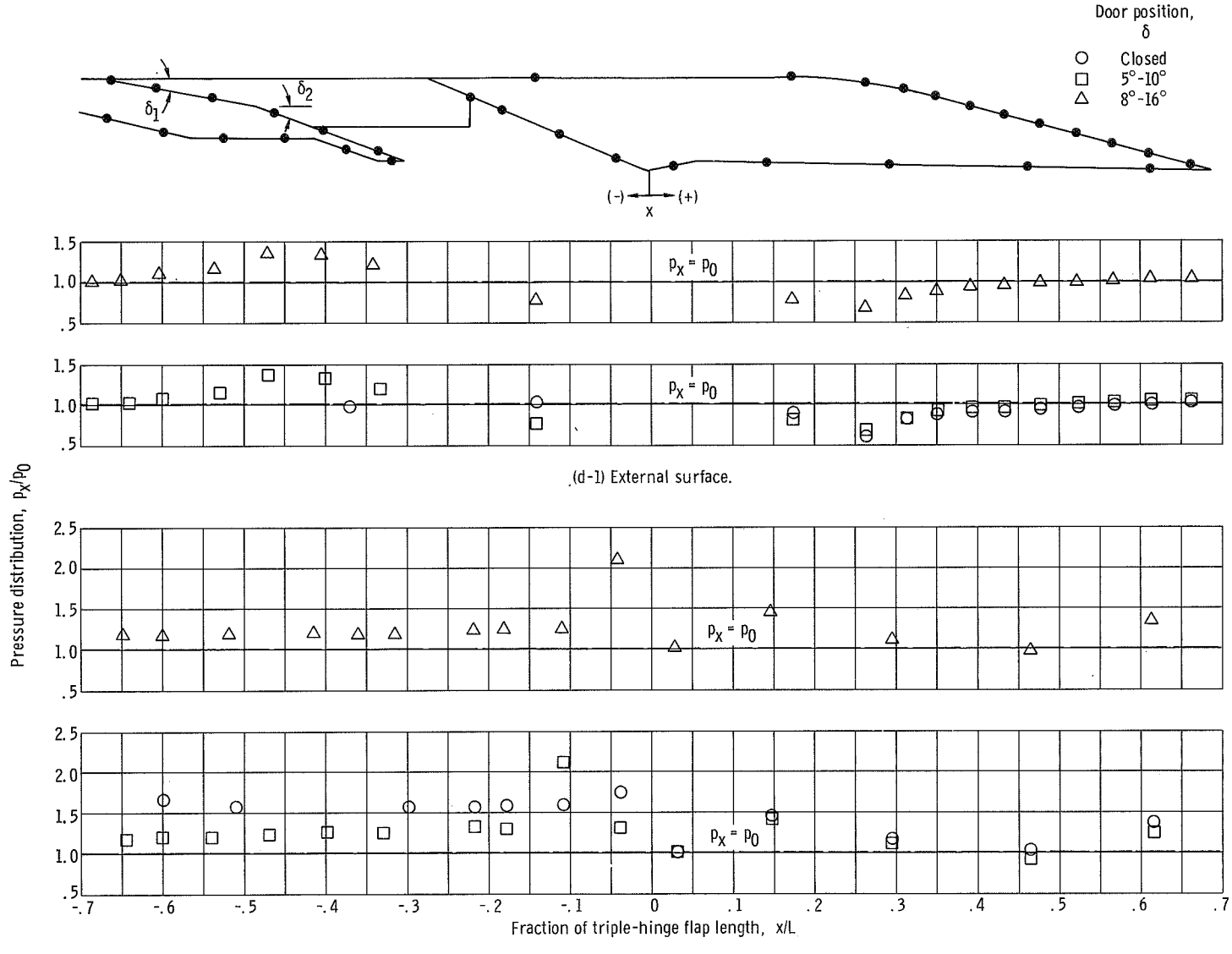

(d-1) External surface.

(d-2) Internal surface.

(d) Maximum reheat acceleration (A_9/A_8 = 1.42); nozzle pressure ratio, P_7/p_0 = 5.6; free-stream Mach number, M_0 = 0.95.

Figure 24. - Concluded.

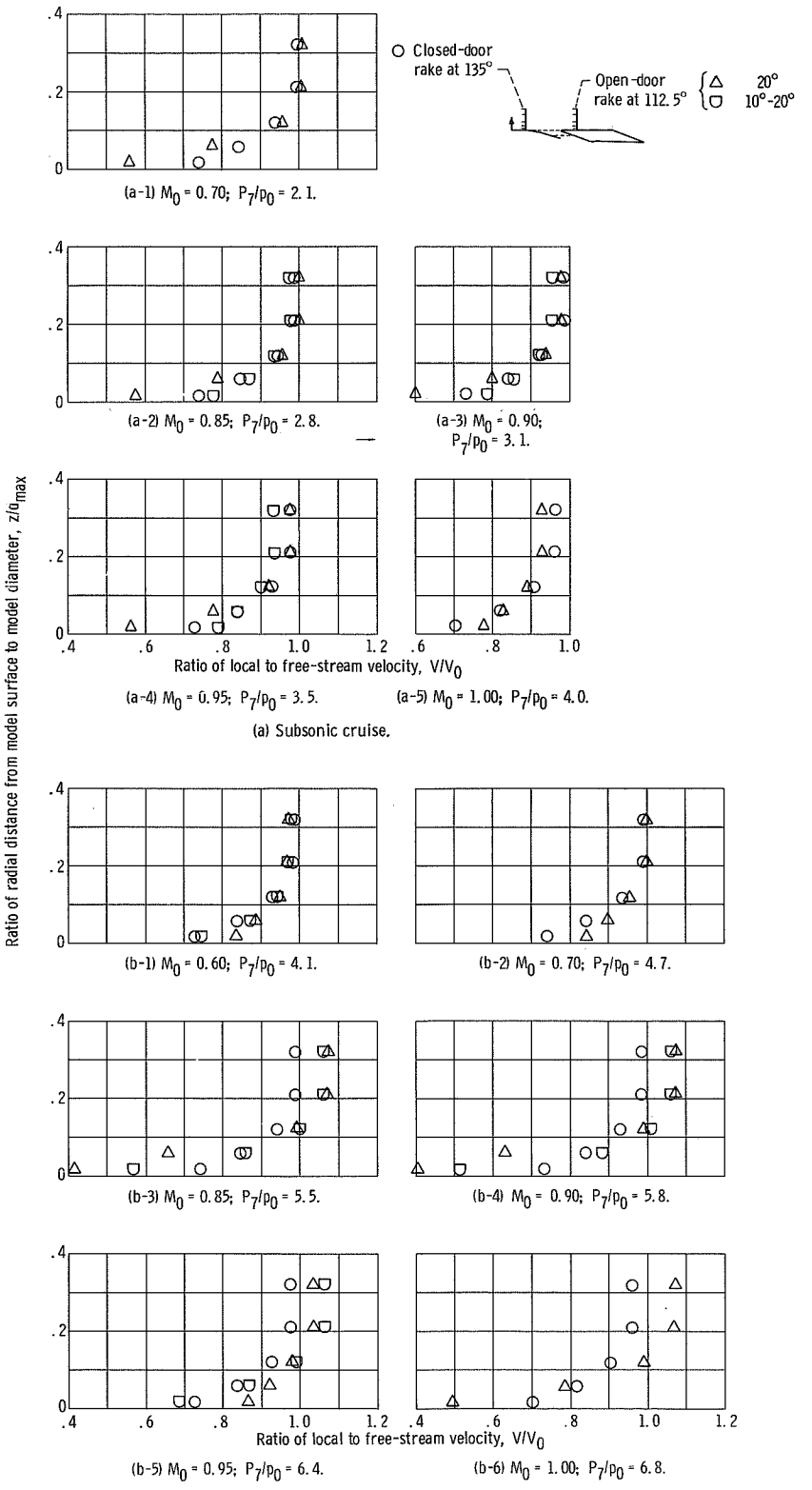

Figure 25. - Comparison of afterbody boundary-layer characteristics for closed and full-open door positions. Corrected secondary-weight-flow-rate ratio, $\omega\sqrt{\tau} = 0.04$; internal area ratio, $A_9/A_8 = 1.99$.

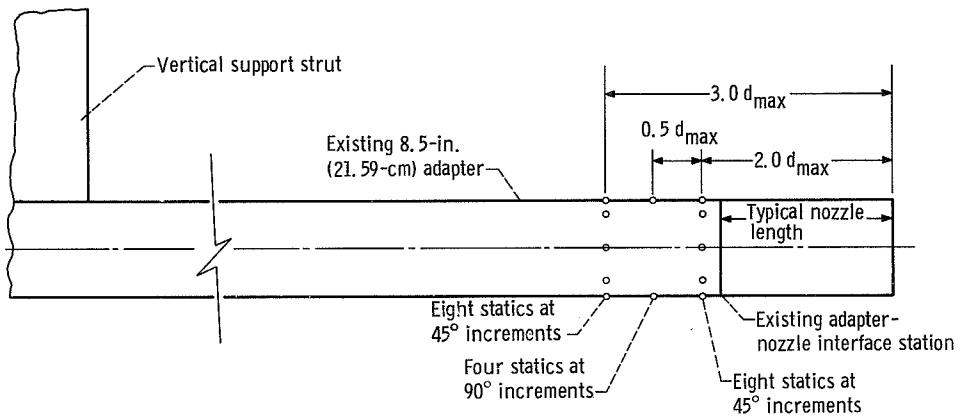

Figure 26. - Location of static-pressure instrumentation on 8.5-inch (21.59-cm) jet-exit model adapter.

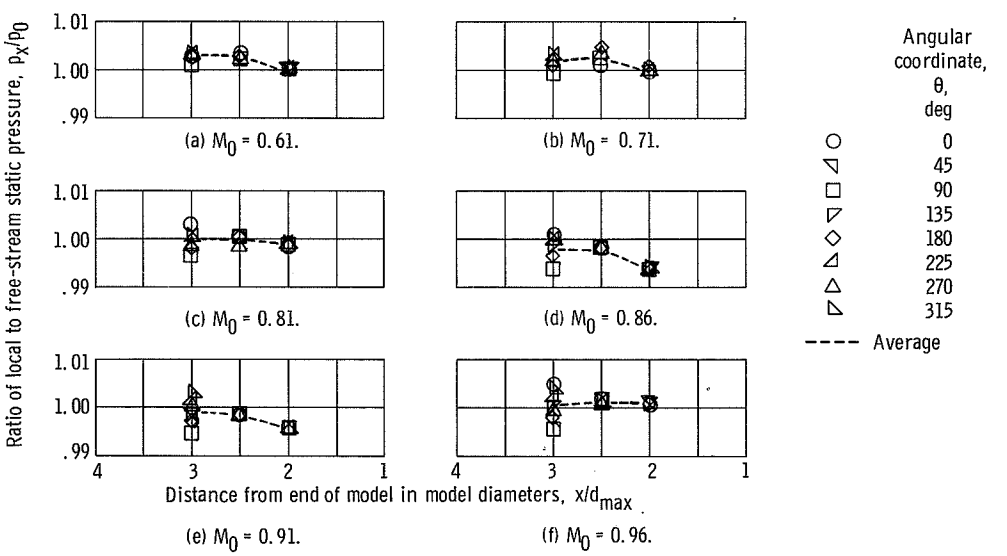

Figure 27. - Static-pressure environment on 8.5-inch (21.59-cm) jet-exit model adapter at subsonic speeds.

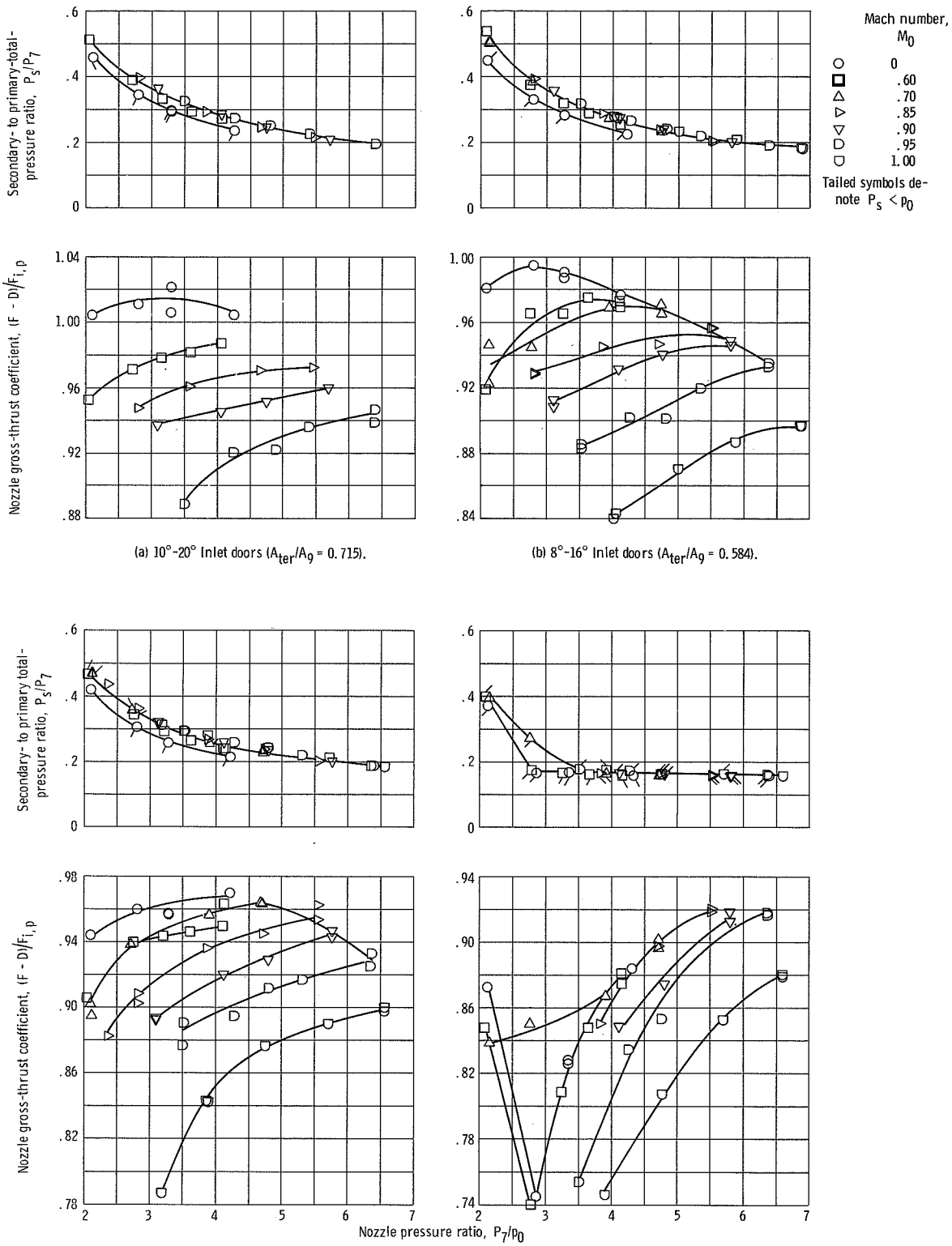

(a) 10°-20° inlet doors (A_{ter}/A_9 = 0.715).

(b) 8°-16° inlet doors (A_{ter}/A_9 = 0.584).

(c) 5°-10° inlet doors (A_{ter}/A_9 = 0.368).

(d) Closed inlet doors (A_{ter}/A_9 = 0).

Figure 28. - Effect of nozzle pressure ratio on nozzle performance characteristics, primary nozzle configuration I (A_9/A_8 = 1.99); corrected secondary-weight-flow-rate ratio, $\omega\sqrt{\tau}$ = 0.026.

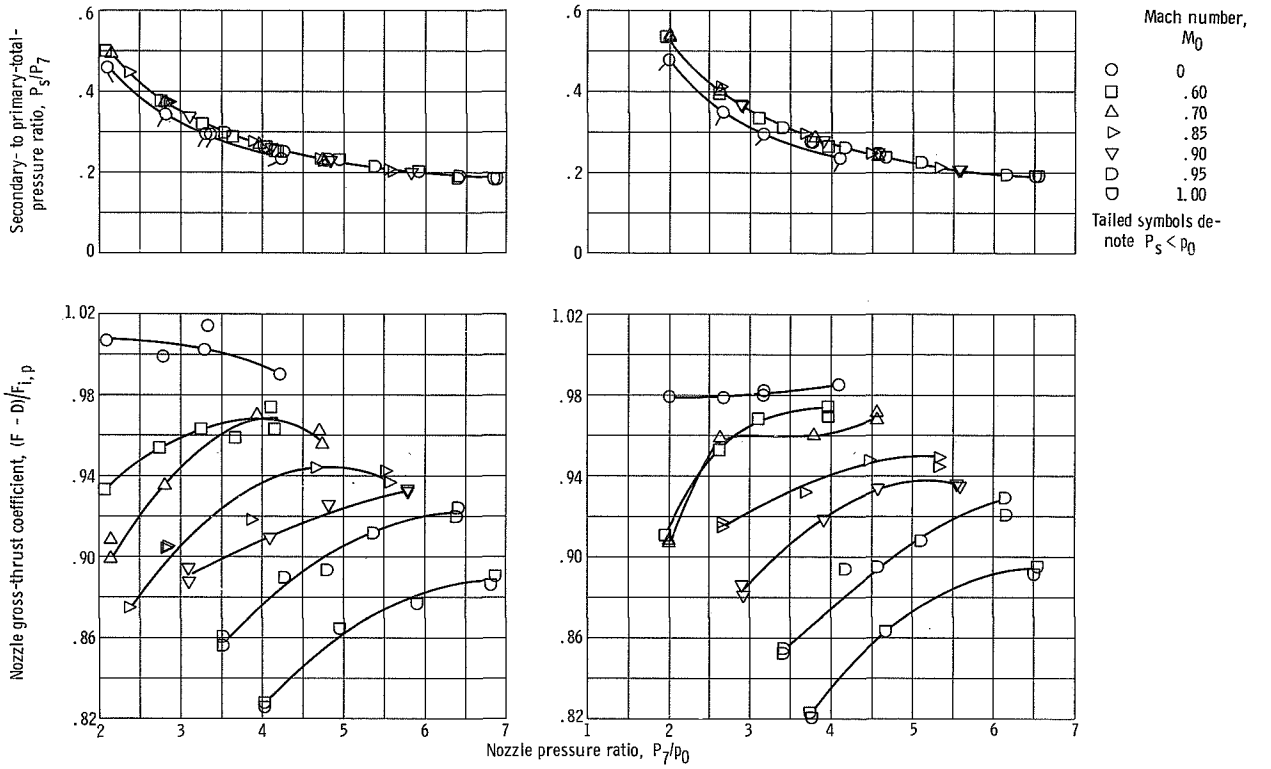

(e) 20° Inlet doors (A_{ter}/A_9 = 0.715).

(f) 16° Inlet doors (A_{ter}/A_9 = 0.584).

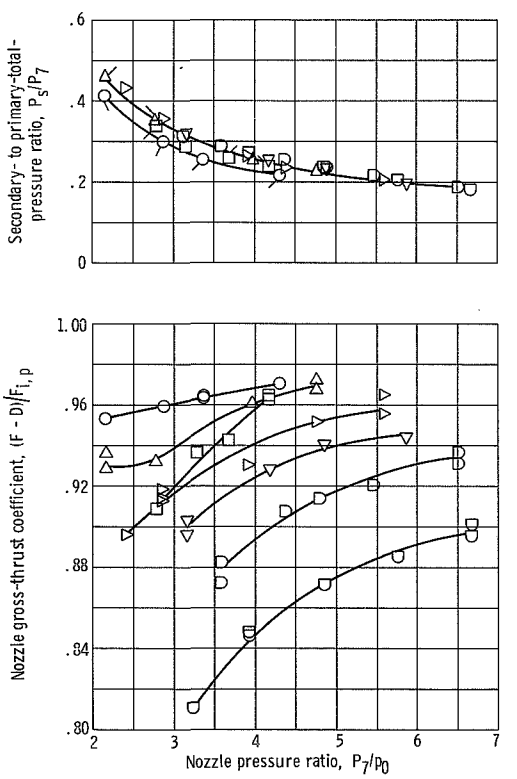

(g) 10° Inlet doors (A_{ter}/A_9 = 0.368).

Figure 28. - Concluded.

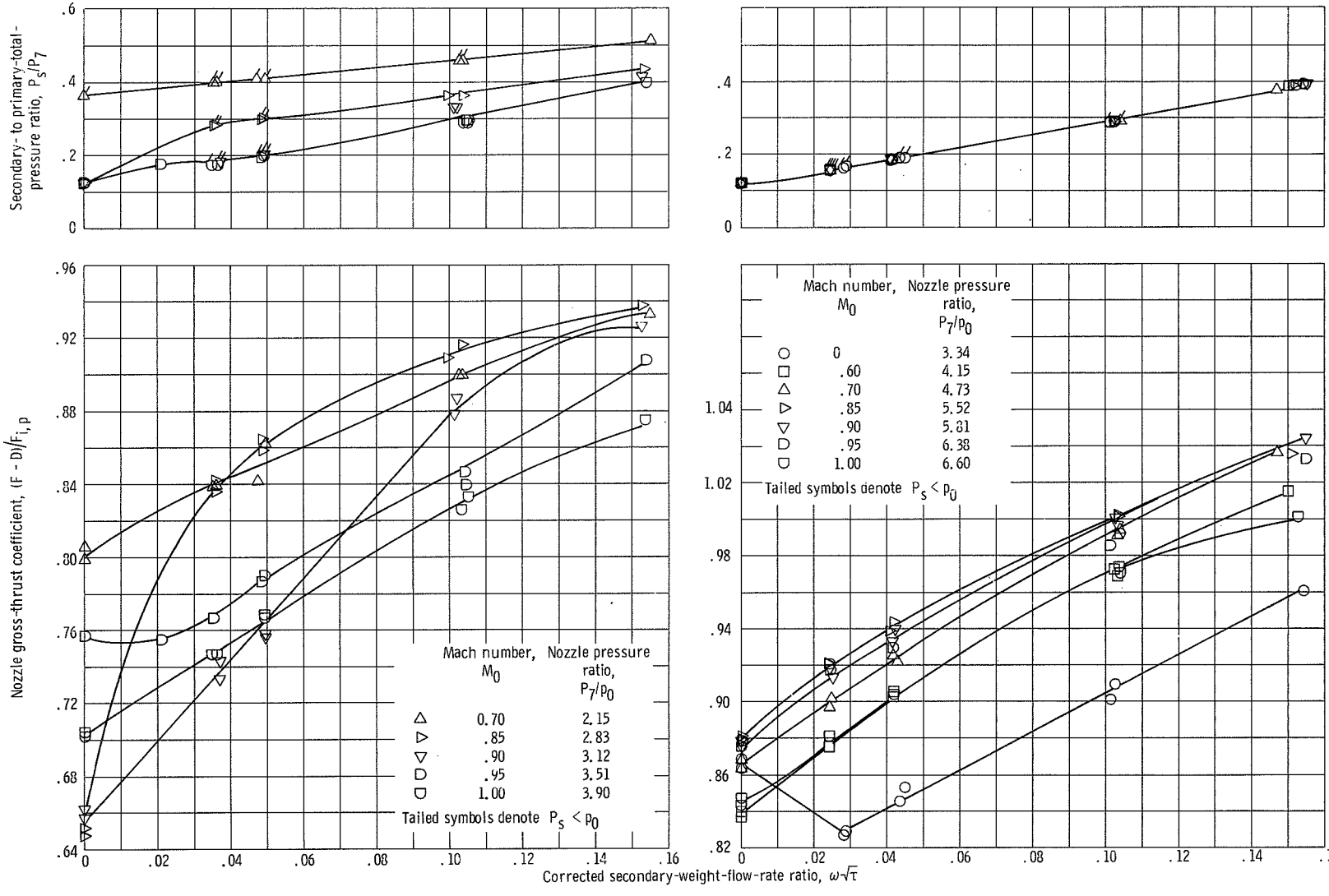

(a) Subsonic-cruise power setting.

(b) Dry-acceleration power setting.

Figure 29. - Effect of corrected secondary-weight-flow-rate ratio on nozzle performance characteristics. Primary nozzle configuration I (A_9/A_8 = 1.99). Closed inlet doors (A_{ter}/A_9 = 0).

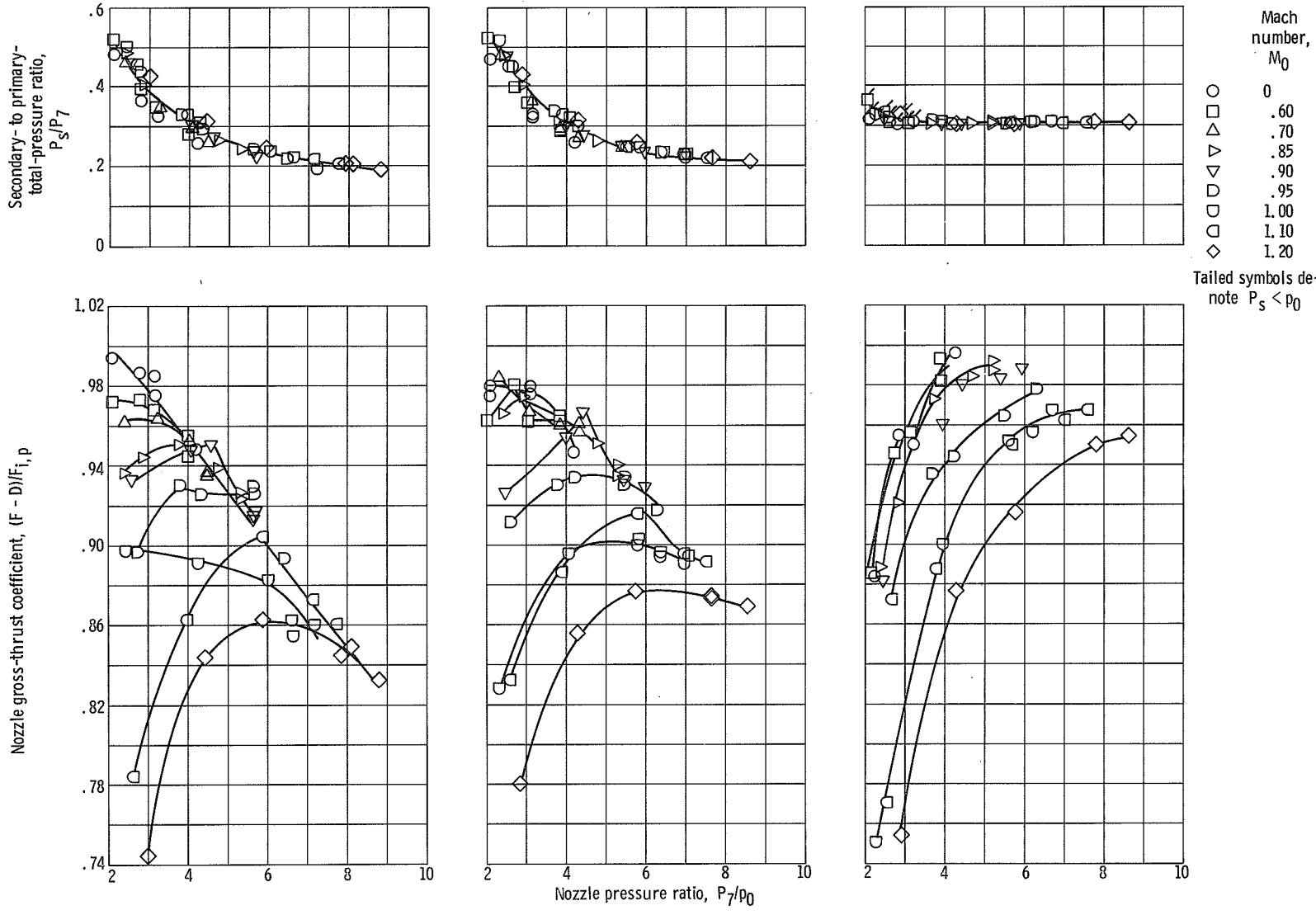

(a) 8°-16° Inlet doors (A_{ter}/A_9 = 0.584).

(b) 5°-10° Inlet doors (A_{ter}/A_9 = 0.368).

(c) Closed inlet doors (A_{ter}/A_9 = 0).

Figure 30. - Effect of nozzle pressure ratio on nozzle performance characteristics. Primary nozzle configuration II (A_9/A_8 = 1.42); corrected secondary-weight-flow-rate ratio, $\omega\sqrt{\tau}$ = 0.04.

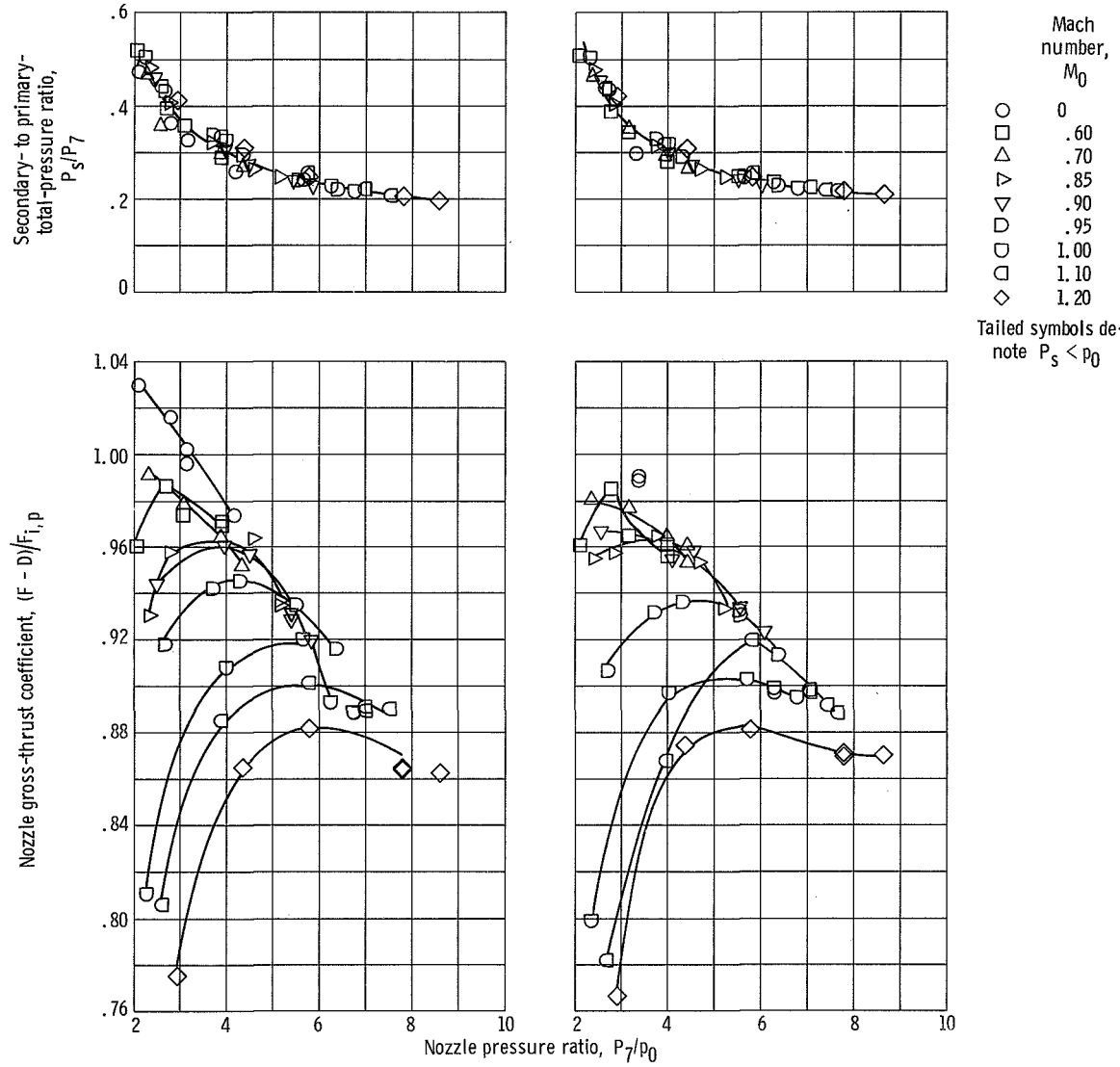

(d) 16° Inlet doors (A_{ter}/A_9 = 0.584).

(e) 10° Inlet doors (A_{ter}/A_9 = 0.384).

Figure 30. - Concluded.

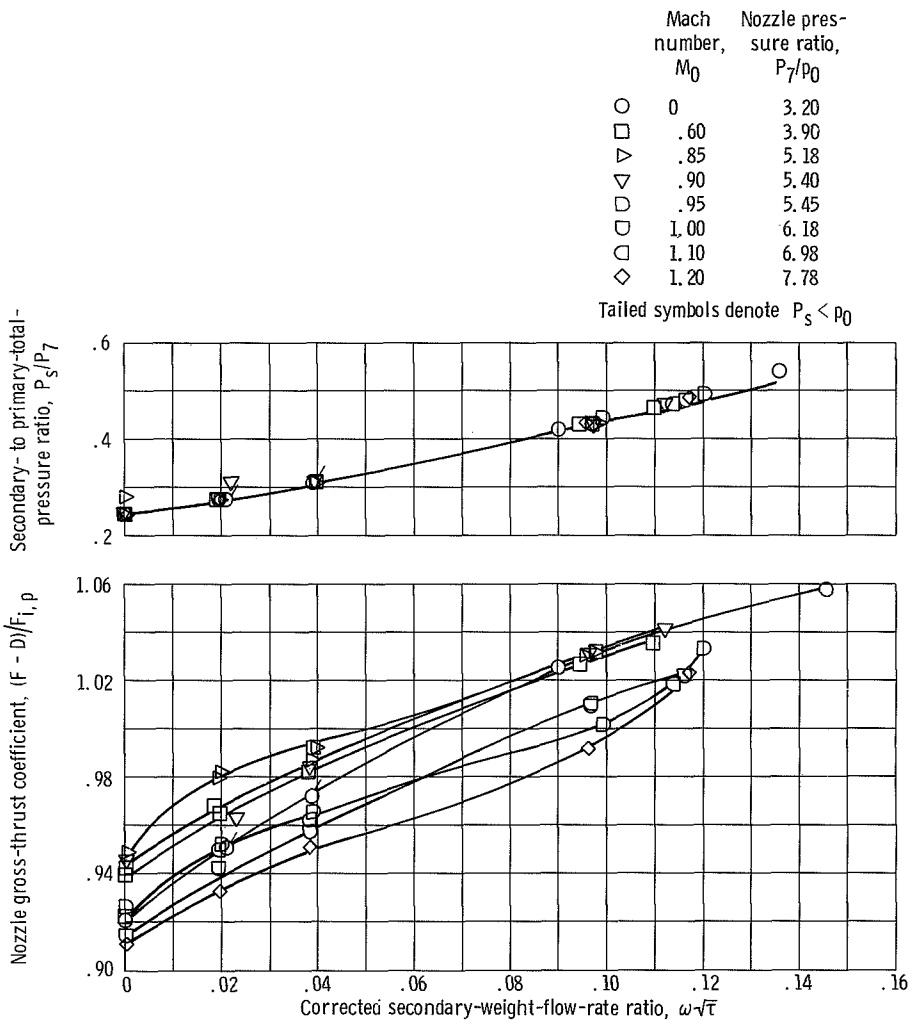

Figure 31. - Effect of corrected secondary-weight-flow-rate ratio on nozzle performance characteristics. Primary nozzle configuration II (A_9/A_8 = 1.42); closed inlet doors (A_{ter}/A_9 = 0).

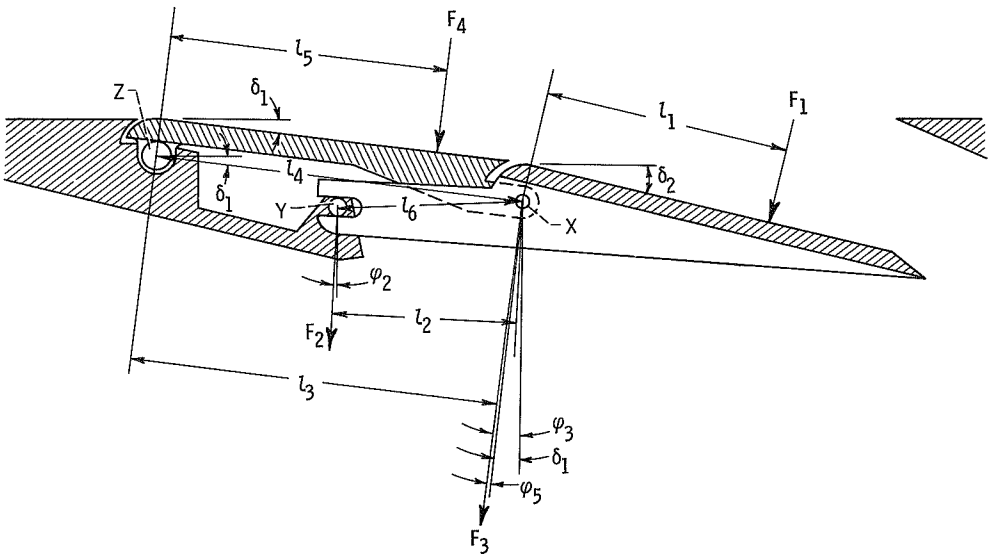

Figure 32. - Assumed mechanism for double-hinge door analysis.

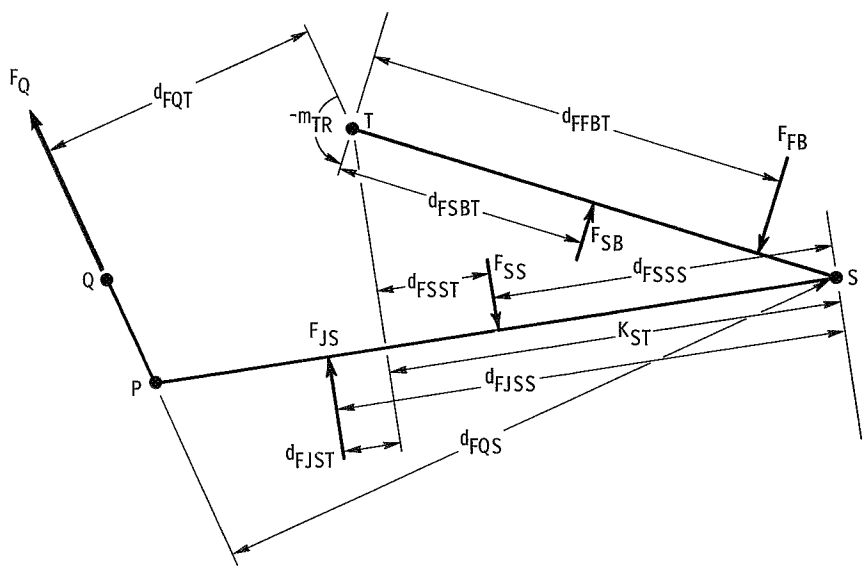

Figure 33. - Schematic sectional view of triple-hinge flap and forces acting upon it.

NASA-Langley, 1970 —— 28 E-5497

NATIONAL AERONAUTICS AND SPACE ADMINISTRATION
WASHINGTON, D.C. 20546

OFFICIAL BUSINESS

FIRST CLASS MAIL

POSTAGE AND FEES PAID
NATIONAL AERONAUTICS A
SPACE ADMINISTRATION

POSTMASTER: If Undeliverable (Section 15
Postal Manual) Do Not Retu

"The aeronautical and space activities of the United States shall be conducted so as to contribute . . . to the expansion of human knowledge of phenomena in the atmosphere and space. The Administration shall provide for the widest practicable and appropriate dissemination of information concerning its activities and the results thereof."

— NATIONAL AERONAUTICS AND SPACE ACT OF 1958

NASA SCIENTIFIC AND TECHNICAL PUBLICATIONS

TECHNICAL REPORTS: Scientific and technical information considered important, complete, and a lasting contribution to existing knowledge.

TECHNICAL NOTES: Information less broad in scope but nevertheless of importance as a contribution to existing knowledge.

TECHNICAL MEMORANDUMS: Information receiving limited distribution because of preliminary data, security classification, or other reasons.

CONTRACTOR REPORTS: Scientific and technical information generated under a NASA contract or grant and considered an important contribution to existing knowledge.

TECHNICAL TRANSLATIONS: Information published in a foreign language considered to merit NASA distribution in English.

SPECIAL PUBLICATIONS: Information derived from or of value to NASA activities. Publications include conference proceedings, monographs, data compilations, handbooks, sourcebooks, and special bibliographies.

TECHNOLOGY UTILIZATION PUBLICATIONS: Information on technology used by NASA that may be of particular interest in commercial and other non-aerospace applications. Publications include Tech Briefs, Technology Utilization Reports and Notes, and Technology Surveys.

Details on the availability of these publications may be obtained from:

SCIENTIFIC AND TECHNICAL INFORMATION DIVISION

NATIONAL AERONAUTICS AND SPACE ADMINISTRATION

Washington, D.C. 20546